University of Southampton

Nanocrystals for resonance energy transfer and lasing applications

by

Mr. Giuseppe Buscemi, M.Sc

A thesis submitted for the degree of Master of Philosophy in the
Faculty of Physical Sciences and Engineering
School of Physics and Astronomy
July 2015

Contents

Introduction **4**

1.1 Resonance Energy Transfer 5

1.2 Nanocrystals for lasing applications 8

1.3 Overview of the thesis 11

Semiconductor Nanocrystals **12**

2.1 Electronic Structure 13

2.2 Synthesis of colloidal nanocrystals 19

2.2.1 Preparation of Monodisperse Semiconductor NCs 19

2.2.2 Preparation NC Core/Shell Structures 21

2.2.3 Synthesis of CdSe/CdS nanorods 22

Resonance Energy Transfer **23**

3.1 Theoretical background 24

3.1.1 Resonance energy transfer 24

3.1.2 Atomic force microscopy 30

3.2 Methodology 36

3.2.1 The laser system 38

3.2.2 Time correlated single photon counting 38

3.2.3 The donor acceptor pair 41

3.2.4 The Tip 43

3.2.5 Controlling the donor acceptor separation 44

3.3 Results 50

3.4 Conclusion 56

Nanocrystal lasing **57**

4.1 Colloidal NCs microsphere laser 58

4.1.1 Introduction 58

4.1.2 Theoretical background 59

4.1.3 Methodology 63

4.1.4 The results 65

4.1.5 Conclusion 67

4.2 Lasing from CdSe QDs embedded in a SiN L3 nanocavity 68

4.2.1 Introduction 68

4.2.2 Theoretical background 69

4.2.3 Methodology 76

4.2.4 Results 80

4.2.5 Conclusion 84

4.3 Chapter Conclusion 84

Appendix **86**

Conclusion 91

Bibliography **92**

DECLARATION OF AUTHORSHIP

I, Giuseppe Buscemi, declare that the thesis entitled "Nanocrystals for resonance energy transfer and lasing applications" has been created by myself as the result of my own original research. I confirm that:

- this work was done wholly or mainly while in candidature for a research degree at this University;
- When I have consulted the published work of others, the source is given.
- I have acknowledged all main sources of help
- Where the thesis is based on work done by myself jointly with others, I have made clear exactly what was done by others and what I have contributed myself

To our misstakkes. May we learn from them

Chapter 1

Introduction

Among the many characteristics that make us human and differentiates us from the rest of the animal world, the pursuit of knowledge is perhaps the most iconic of all. To survive at first. Learning the behavior of animals to better hunter them for example, but also to satisfy our need for curiosity-driven answers. What are the stars? What is a thunder? To answers those questions about the natural world, religion arose first as explanation. Gods related to the natural world were created. Then, after several millennia, philosophy tried a different approach to answer the very same questions and more elaborate explanations were suggested, sometime even quite close to what we know today to be true. Finally, in the Renaissance, the true scientific method (observation, hypothesis, experiment to prove the hypothesis or disprove it) was elaborate by Galileo Galilei, embraced by the

protestant word at first, and since those days has led us to the moon and beyond.

In this work we are going to explore the use of a particular kind of nanomaterial, called nanocrystals (NCs), for resonance energy transfer (RET) and lasing applications. NCs have already been researched in the early 1980's [1,2] however it has not been until the early 1990's that reliable methods of production were developed [3].

Colloidal semiconductor nanocrystals are a subclass of NCs synthesized from precursor compounds dissolved in solutions. They are very interesting because of their excellent spectral tunability in the emission spectrum, from the visible to the near infrared, just by changing their size and shape [4]. Today they are used in applications from fluorescent labels [5] through spintronics [6] and photovoltaic [7] to light emitting diodes [8] and photodetectors [9]

1.1 Resonance Energy Transfer

In this work the creation of a novel technique to study resonance energy transfer (RET) distance dependence, in the few nanometers range and without altering the sample, is investigated.

The simplest way to perform a distance dependence, where applicable, is to grow a spacer between the two specimens we want to separate. In ref. 10 the Nakayama research group used layer-by-layer assembly of polyelectrolytes to control the separation distance between two layers of quantum dots (QDs). This approach, although relative precise with a resolution of 1 nm, has the drawback of the need of several samples, one for each separation point. This is not a concern when the research is performed used commercial available QDs and very easy to build samples but can easily became a major obstacle when more complicated and expensive samples are required. A similar approach has been used in ref. [11] where in order to study the RET distance dependence, three different quantum well (QW) samples, with three different capping layers on top the QWs have been produced. In order to study only three separation distance 3 QWs were made.

To overcome this limitation the use of atomic force microscopy (AFM) has been introduced in recent years. In 2004 the Benson group investigated the RET between CdTe Nanocrystals on Polystyrene Beads and Dye Molecules using a near field spectroscopy tip (SNOM) [12]. In this study they attached a polystyrene bead coated with CdTe NCs to a SNOM tip and studied the RET in contact for two different regimes of the AFM machine that drives the SNOM tip: strong damping and shear-force. In the first case the sinusoidal amplitude oscillation of the tip was 3nm and in the second case 15nm. Using this approach they were able to measure RET distance

dependence for two points, where accuracy in the separation distance was not provided anymore by a capping layer but by the AFM equipment capabilities.

However this method has still some drawbacks. There is no real control of the separation distance and is not possible to change the separation distance once the driven force for the SNOM's tip has been selected.

With the evolution of the AFM technology more control over the distance separation has been acquired. In 2010 and 2011 RET between QDs and carbon nanotube [13] and CdSe/ZnS core/shell nanocrystallite quantum dots [14] has been observed as function of distance, in the range 10nm to 50+ nm, using a SNOM tip. Although both groups were able to correlate the RET as function of the separation distance between specimen, none of them were able to choose or select the different steps in the distance dependence. Moreover there was no information below 10nm, where most of the RET takes place. This work tackles this missing part of the RET distance dependence studies.

1.2 Nanocrystals for lasing applications

The second important aspect of this work investigates how the NCs can be used, in a variety of form, to produce micro-lasing devices. In particular two configurations have been investigated.

The first configuration uses uncoated silica microsphere, as resonator, and a CdSe/CdS NRs coated angle polished optical fiber to archive lasing regime. Whispering gallery modes (WGM) and doped microsphere resonators have been used since the 90' to archive lasing regime. In 1996 Sandoghdar et al. [15] reported the realization of a whispering-gallery-mode laser based on neodymium-doped silica microspheres with a threshold as low as 200 nW. In 2000 Cai et al. [16], using an highly doped erbium-ytterbium phosphate glass microsphere, reached single mode lasing using a tapered fiber to excite and collect the lasing signal. Both approaches present however some drawbacks: very low tunability of the lasing and the need to use doped glass. But more important is not possible to archive single particle lasing this way.

Theoretical calculations of a single particle lasing regime that use an uncoated silica microsphere were performed in 1999 by the Yamamoto group [17]. They showed that was possible to create a semiconductor micro-laser by capturing the light emitted from a single InAs/GaAs quantum dot in the whispering-gallery mode of a glass microsphere. Following this approach in 2007 Steiner et al. [18] claimed to have archived lasing regime with a prism

excitation/collection method, using less than 100 NCs per mode, on a mesa structure brought in close proximity of the microsphere. Lasing emission was clear but in the paper they stated that because the difficulty to bring the mesa close to the surface and keep it stable (and the author of this work really agrees on how difficult is to have this very close proximity without touching the microsphere), they simply brought in contact the mesa with the microsphere. In doing this contamination of the uncoated silica microsphere is very likely, especially with a calculated number of QDs lasing below 100. Our approach to archive lasing without coating the microsphere differs in the configuration. In this work an angled polished fiber coated with CdSe/CdS NCs is brought close to the uncoated silica microsphere without never touching it. In this way laser regime has been achieved.

The second configuration in this work uses a photonic crystal (PC) as resonator instead of a microsphere. Photonic crystals are periodic optical nanostructures that affect the motion of photons in much the same way that ionic lattices affect electrons in solids and in recent years have surged to a huge variety of form, class, type and applications. Perhaps the most famous commercial application of photonic crystal are photonic crystal fibers. Two dimensional photonic crystals nanocavities (2D PC), are optical structures that confine light. Strong confinement makes them attractive to explore a range of fundamental phenomena such as the Purcell effect [20], ultralow threshold lasers [21] and optical nonlinear effects [22]. So far, most progress

has been focused on fabricating structures based on III-V semiconductors. However, exciton emission from III-V semi-conductors can only be generated at cryogenic temperatures, with emission limited to near infrared. For example in 2006 a near infrared lasing using 2-4 QDs embedded in 2D PC was achieved but at cryogenic temperature [23].

In recent years silicon nitride (SiN) has emerged as a promising material with photoluminescence and electroluminescence generated at visible wavelengths at room temperature. Makarova et al. [24] have experimentally studied the emission properties of L3 SiN-based nanocavities and were able to demonstrate cavities having quality factors in the range 200–300. Barth et al. [25] have theoretically and experimentally investigated the optical properties of L3 SiN nanocavities coated with the fluorescent molecular dye Nile Red as a function of the displacement of the two holes neighboring the nanocavity. Murshidy et al. [26] report the fabrication of L3 SiN nanocavities membrane coated with a thin10 nm film of fluorescent red-emitting conjugated polymer observing an enhancement of the PL emission of the polymer.

In this work, we investigated, at room temperature, a L3 SiN membrane coated with CdSe QDs embedded in the nanocavity. QDs are spincoated on the PC and lasing regime has been observed.

1.3 Overview of the thesis

The work at hand is structured into four chapters, the first of which is this introduction. An appendix explains a small experiment on a different topic of research that differs from the core of this thesis.

The second chapter explains the physics of semiconductor crystals and semiconductor nanostructures. Introduces the mathematical framework to describe the exciton in semiconductor nanostructures.

Chapter three outlines the mechanism of RET and is dedicated to the experimental and theoretical methods we employed during our research. We present the technique that has allowed us to perform a RET distance dependence study, the AFM equipment, the laser system and time resolved spectroscopic techniques that allowed us to investigate the exciton structure and dynamics in our material system and our results.

Chapter four shows the theoretical background, the experimental methods and equipment we used to archive lasing with NCs. The theory of whispering gallery modes and photonic crystal is explained and we describe how, using NCs, silica microsphere resonator and PC nanocavity, we achieved lasing regime in both configurations.

The appendix shows an evanescence field spectroscopy experiment in which tapered fibers and golden nanoparticles have been used to realize an extremely sensitive device based on evanescence spectroscopy.

Chapter 2

Semiconductor Nanocrystals

In this work we deal with several applications of semiconductor nanocrystal, both in the class of pure spherical quantum dots and elongated nanorods. This chapter is devoted to the introduction of the investigated material systems and their synthesis. To understand the properties of the material system we will first discuss the concept of a semiconductor and then explain the effect of conferment of carriers in semiconductors. Then we will discuss the crystal structure of CdSe and the influence of the crystal surface on the colloidal growth of heterostructured NRs. Following that we will introduce the chemical synthesis of spherical NC and heterostructured NRs. There we show the critical influence of the surface energy for the formation of asymmetric NRs.

2.1 Electronic Structure

"There is plenty of room at the bottom…in the science of ultra-small structures" was a famous statement of R. Feymann at a talk given in the year 1959 [27]. In this talk R. Feymann described his vision of fantastic and numerous possibilities if one could control the size and dimension of objects in the nanometer range and thus create objects with completely new properties lying in between atoms/molecules and solids. Nanoparticles are located at this junction between atoms/molecules and solids consisting of 100 to 10,000 atoms. Going from a solid 'infinite' crystal to an atom the density of states change from continuous bands to discrete energy levels. As the energy levels of nanocrystals lie in between atoms/molecules and solid 'infinite' crystals, their electronic properties are size dependent. For semiconductors the Fermi level is located between two bands, therefore the optical and electronic properties are mainly dominated by the edges of the energy bands. As the edges of a band develop last, even for relatively large particles (around 10,000atoms) discrete energy levels are observed [28]. The change in electronic and optical properties observed in semiconductor nanoparticles relative to the semiconductor solid material is called quantum size effect. Semiconductor nanoparticles that show a quantum size effect are called quantum dots. Figure 2.1 illustrates the effect of reduced dimension in a semiconductor. The energy levels become discrete near the energy level when going from an infinite "3D"crystal to a "0D"quantum dot [29]

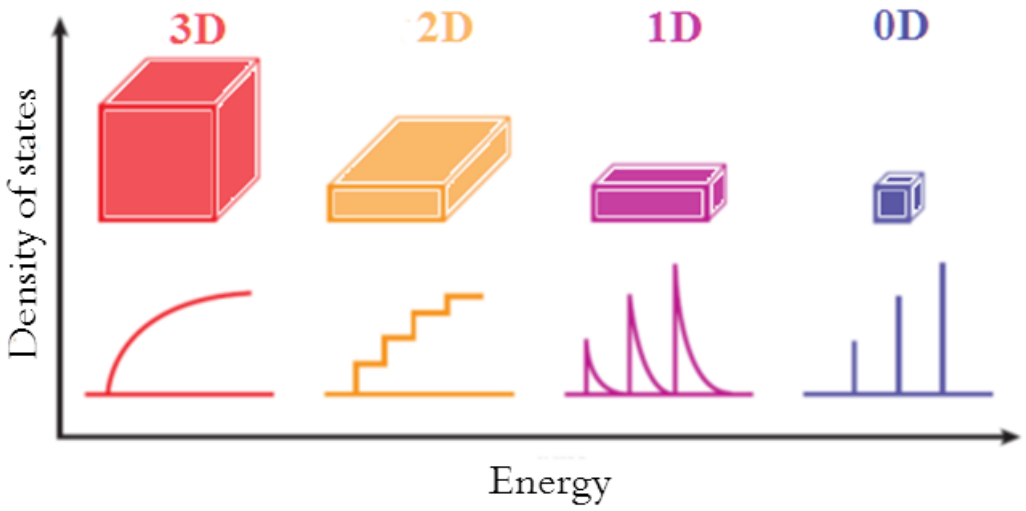

Fig. 2.1 Density of states in a semiconductor as a function of dimension [29]

The discrete energy levels for electrons in a quantum dot, can be described by quantum mechanics in the easiest case as an electron in a spherical potential well with infinite barriers. The solution of the time independent Schrödinger equation is the wave function of the electron [29]

$$\left[\frac{-\hbar^2}{2m_e}\nabla^2 + U(r)\right]\Psi(r) = E\,\Psi(r) \qquad (2.1)$$

Where E and U(r) are total and potential energies, m_e the electron effective mass, and $\hbar$ is the reduced Plank constant. By applying the Hamilton operator

$$H = \left[\frac{-\hbar^2}{2m_e}\nabla^2 + U(r)\right] \qquad (2.2)$$

On the wave function the eigenvalues E_n and therefore the allowed energy states of the electrons are obtained. The potential energy U(r) depends solely on the distance $r = \sqrt{x^2 + y^2 + z^2}$ and is

$$U(r) = \begin{cases} 0, & \text{for } r < a \quad (2.3a) \\ \infty, & \text{for } r \geq a \quad (2.3b) \end{cases}$$

where a is the radius of the quantum dot. The Laplace operator $\Delta = \nabla^2$ in spherical coordinates includes radial and spherical parts, the radius r the azimuth angle $0 \leq \varphi \leq 2\pi$ and the polar angle $0 \leq \theta \leq \pi$ and consists of [29]

$$\Delta = \nabla^2 = \nabla_r^2 + \frac{1}{r^2} \nabla_{\varphi\theta}^2 \quad (2.4)$$

Therefore the Schrödinger equation for an electron in a spherical potential can be written as [29]

$$\left[\nabla_r^2 + \frac{1}{r^2}\nabla_{\varphi\theta}^2 + \frac{2m_e}{\hbar^2}(E - U(r))\right]\Psi(r, \varphi, \theta) = 0 \quad (2.5)$$

The wave function can be separated into a radial- and an angle-dependent function $\Psi(r, \varphi, \theta) = X(r)Y(\varphi, \theta)$ as the potential U(r) is independent of the angle. Using the boundary condition that the wave function has to vanish for r = a and equation 2.5 a solution for the radial function X(r) is

$$X(r) = \sqrt{\frac{2}{a}} \frac{\sin(kr)}{r} \quad (2.6)$$

With $k = g_{nl}/a$. g_{nl} are the roots of the corresponding Bessel function. The boundary condition that X(r) has to vanish for r = a leads to a quantization and to three new quantum numbers n = 1,2,3 ….. l = 0,1,2,3 …. and m= 0, ± 1, ± 2, …. ± l, where l is called the orbital quantum number and therefore the states l = 0, l = 1 and l = 2 are called analogous to atomic orbitals s, p and

d and m is the orbital magnetic quantum number. The resulting energies of an electron in the allowed stationary states are:

$$E_{nl} = \frac{\hbar^2}{2m_e a^2} g_{nl}^2 \tag{2.7}$$

where m_e is the effective mass of the electron. Therefore the energy of the electron in a quantum dot has discrete values and scales with the inverse square of the quantum dot radius *a*. As g_{10} equals π, the lowest energy of an electron in an allowed state is therefore

$$E_{10} = \frac{\hbar^2}{2m_e a^2} \pi^2 \tag{2.8}$$

Equation 2.6 and 2.7 give the confinement energy of an electron in a quantum dot with a radius *a*. To get an estimation of the energy of optical transitions in quantum dots one has to consider the macro crystalline band gap of the material plus the confinement of the electron in the conduction band and the hole in the valence band, which form during absorption. Therefore the easiest estimation for the transition of the first excitonic peak, where n = 1 and l = 0 is

$$E = E_{gap} + E_{10}^e + E_{10}^h = E_{gap} + \frac{\hbar^2 \pi^2}{2a^2}\left(\frac{1}{m_e} + \frac{1}{m_h}\right) \tag{2.9}$$

where m_h denotes the effective mass of the hole. The energy of the first excitonic peak is changed by the Coulomb attraction between electron and hole and by the solvation energy induced by the surrounding medium

$$E = E_{gap} + E_{10}^{e} + E_{10}^{h} - E_{Coulomb} + E_{sol} =$$

$$= E_{gap} + \frac{\hbar^2\pi^2}{2a^2}\left(\frac{1}{m_e} + \frac{1}{m_h}\right) - \frac{1.8}{\varepsilon_{in}}\frac{e^2}{4\pi a\varepsilon_o} - \tag{2.10}$$

$$- \frac{e^2}{4\pi a\varepsilon_o} + \frac{e^2}{a}\sum_{n=1}^{\infty}\frac{\left(\frac{\varepsilon_{in}}{\varepsilon_{out}} - 1\right)(n+1)}{\varepsilon_{in}\left(\frac{\varepsilon_{in}}{\varepsilon_{out}} + n + 1\right)}\left(\frac{S}{a}\right)^{2n}$$

Where ε_{in} and ε_{out} are the dielectric constants of the quantum dot and the surrounding medium, respectively, e is the elementary charge, and S is the magnitude of the distance that the wave function peaks from the center of the spherical particle. Table 2.1 lists the electronic parameters of a few selected crystalline direct band gap semiconductors. The effective electron and hole mass are in units of the free electron mass

	Egap (eV)	m_e	m_h	ε_{in}
CdTe	1.43	0.11	0.41	7.1
GaAs	1.52	0.07	0.68	10.9
CdSe	1.75	0.13	0.45	5.8
CdS	2.58	0.19	0.80	5.7
ZnO	3.44	0.24	0.45	3.7

Table 2.1 Band gap (Egap), effective electron (m_e) and hole mass (m_h) and the optical dielectric constant of a few selected crystalline direct band gap semiconductors [30, 31]

Table 2.2 shows the energy shifts of the first excitonic peak of QD with a diameter of 6nm relative to the band gap of the bulk semiconductor. The values calculated with equation 2.9 and the electronic parameters given in table 2.1. The calculations were done for QD in vacuum therefore $\varepsilon_{out} = 1$

and S/a was set to 0.2. The total shifts varied between 0.09 eV and 0.59 eV, while the kinetic energy had the biggest share and the influence of the solvation energy was minor

	E_{Kin}	$E_{Coulomb}$	E_{Sol}	E_{total}
CdTe	0.48	-0.12	0.05	0.41
GaAs	0.66	-0.11	0.04	0.59
CdSe	0.41	-0.15	0.05	0.32
CdS	0.27	-0.15	0.05	0.17
ZnO	0.27	-0.23	0.06	00.09

Table 2.2 Energy shifts of the first excitonic peak in QDs of selected semiconductors (d = 6 nm) due to the kinetic energy ($E_{kin} = E_{10}^{e} + E_{10}^{h}$), the Coulomb energy ($E_{Coulomb}$) and the solvation energy (E_{Sol}) summing up to a total shift E_{total}. The energy values are given in eV [31]

Aside from providing the possibility of confining excitons, NCs also allow for intrinsic spatial separation of the constituting electron and hole. By synthesizing nanostructures of two or more materials with different band gaps one can design different spatial areas of confinement for the constituent carriers. Core shell semiconductor nanocrystal properties are based on the relative conduction and valence band edge alignment of the core and the shell. In type I semiconductor heterostructures, the electrons and holes tend to localize within the core. In type II heterostructures, one carrier is localized in the shell while the other is localized in the core.

2.2 Synthesis of colloidal nanocrystals

The production of colloidal QDs requires a temporally discrete nucleation event followed by slower controlled growth on the existing nuclei. Rapid addition of reagents to the reaction vessel raises the precursor concentration above the nucleation threshold. A short nucleation burst partially relieves the supersaturation. As long as the consumption of feedstock by the growing colloidal NCs is not exceeded by the rate of precursor addition to solution, no new nuclei form. Since the growth of any one NC is similar to all others, the initial size distribution is largely determined by the time over which the nuclei are formed and begin to grow [32]. If the percentage of NC growth during the nucleation period is small compared with subsequent growth, the NCs can become more uniform over time. This phenomenon has been referred to as focusing of the size distribution.

2.2.1 Preparation of Monodisperse Semiconductor NCs

In the growth of compound semiconductor NCs, the requisite supersaturation and subsequent nucleation can be triggered by rapid injection of metal-organic precursors into a vigorously stirred flask containing a hot (150–350 C) coordinating solvent. The solvents usually used are mixtures of long-chain alkylphosphines R3P, alkylphosphine oxides R3PO, alkylamines ect. A representation of the synthetic process is shown in Figure 2.2.1

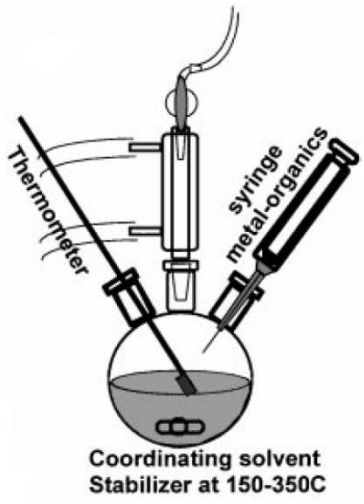

Fig. 2.2.1 Representation of the simple synthetic apparatus employed in the preparation of monodisperse NC samples. [32]

In the synthesis of II–VI NCs metal alkyls are generally selected as the group II sources. The group VI sources are often organophosphine chalcogenides (R3PE) orbistrimethylsi–lylchalcogenides TMS2E (TMS, trimethylsilyl) (where EDS, Se, and Te).TheR3PE class of reagents is usually preferred as Se and Te sources because they are easy to prepare; TMS2S is selected as the S source because it is more reactive thanR3PS and is commercially available. The use of mixed precursors, for example a combination of Se and S precursors, leads to the straightforward production of alloys, although the NCs' stoichiometry does not directly reflect the precursor ratio, but rather the differential rate of precursor incorporation. Similarly, synthesis of high–quality InP and InAs NCs has been achieved by rapidly mixing and heating of III and V precursors in high boiling, coordinating solvents [32].

2.2.2 Preparation NC Core/Shell Structures

The techniques to overcoat NCs with an inorganic shell are general with only a few modest constraints:

1. The existing NC seeds must withstand the conditions under which the second phase is deposited
2. The surface energies of the two phases must be sufficiently similar so that the barrier for heterogeneous nucleation of the second phase is lower than that for homogeneous nucleation
3. The seed NC and the overcoat material must not readily interdiffuse under the deposition conditions

Typically seed NCs are prepared and isolated by one of the standard procedures outlined above, size selected, and then re-dispersed in a fresh solution of solvent and stabilizers. The solution is then heated while precursors for the inorganic shell are gradually added to allow the material to heterogeneously nucleate on the seed NCs. If the rate of precursor addition does not exceed the rate of deposition on the seeds, the precursor concentration never reaches the threshold for homogeneous nucleation of a second inorganic phase. Methods for overcoating a semiconductor NC with a second semiconductor material of wider bandgap are well developed. For example, CdSe nanocrystalshave been overcoated with ZnS, ZnSe, and CdS, which resulted in dramatic improvements in luminescence efficiency.

2.2.3 Synthesis of CdSe/CdS nanorods

The synthesis of the CdSe/CdS NRs used in this work is based on the co-injection of appropriate precursors and preformed spherical CdSe nanocrystal seeds (nearly monodisperse in size) in a reaction flask that contains a mixture of hot surfactants suited for the anisotropic growth of CdS nanocrystals [33]. In a typical synthesis of nanorods reported in this work, CdO is decomposed in the presence of a mixture of trioctylphosphine oxide, hexylphosphonic acid, and octadecylphosphonic acid in relative ratios that have been carefully optimized. The resulting solution is heated to 350-380 °C under inert atmosphere. Separately, a solution is prepared by dissolving sulfur in trioctylphosphine and by adding to it either CdS or CdSe nanocrystals (previously prepared and purified). This solution is quickly injected in the flask, after which the temperature of the flask is allowed to recover to its pre-injection value and the synthesis is kept running for several minutes before stopping it by removing the heating mantle. Immediately after injection, CdS starts growing preferentially on the CdSe seeds rather than forming separate nuclei in solution because the activation energy for heterogeneous nucleation is much lower than that for homogeneous nucleation. As the homogeneous nucleation is bypassed by the presence of the seeds, all nanocrystals undergo almost identical growth conditions and therefore they maintain a narrow distribution of lengths and diameters during their evolution.

Chapter 3

Resonance Energy Transfer

The following sections are dedicated to the description of the work done with the NCs and the AFM/SNOM equipment to study the resonance energy transfer distance dependence (RET).

At first we introduce the basically principles of the RET and AFM, the laboratory setup that was used to perform the time resolved spectroscopic experiments, the laser system and the time-correlated-single-photon-counting (TCSPC) setup that we used to record the NC decay data. Then we explain more in details the technique that has allowed us to control the separation distance and then we present our results.

3.1 Theoretical background

3.1.1 Resonance energy transfer

Resonance energy transfer is a distance-dependent interaction between the electronic excited states of a donor-acceptor system, in which excitation is transferred from the lower excited state of the donor to a higher energy excited state of the acceptor without emission of a photon.

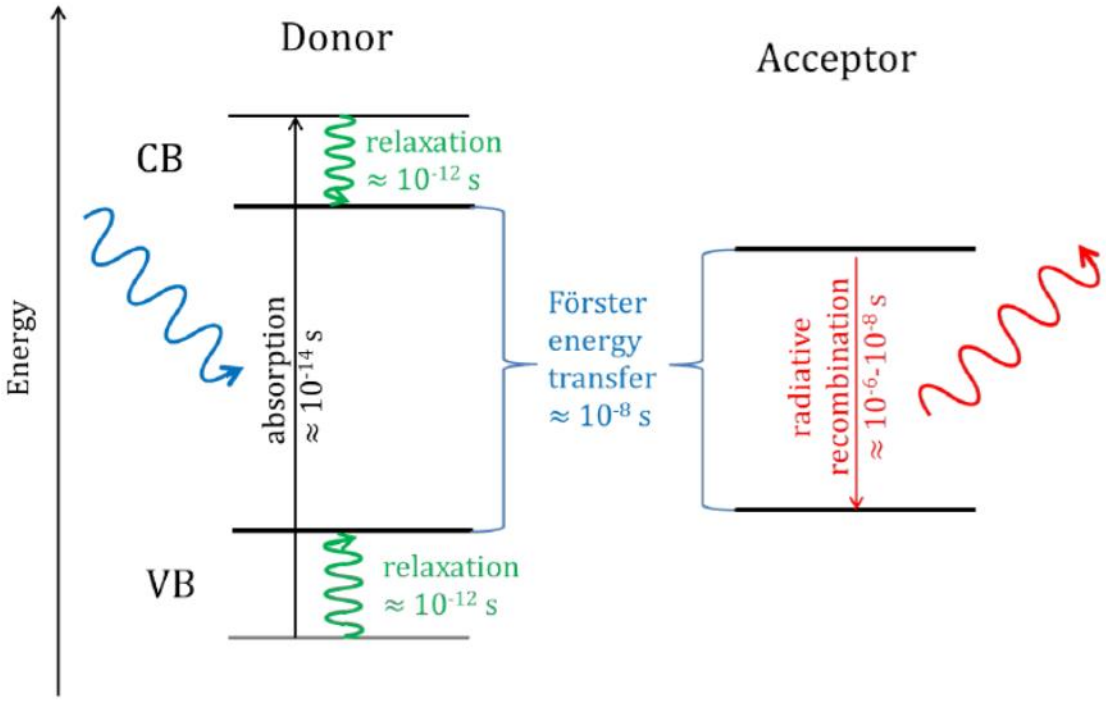

Fig. 3.1.1 Scheme of the Förster energy transfer and radiative recombination

In the early 20' of the last century, Cairo et al. found a non-radiative dipole–dipole model that successfully accounted for energy transfer in gas mixtures arising from near collision processes between the atoms [34, 35]. It

was found that energy could be transferred over distances beyond the hard core collision distances between molecules, in the near-field zone of dipole–dipole interactions.

The Perrins, father and son, were the first to attempt a quantitative description of nonradiative (without emission of a photon) energy transfer in solution between an excited molecule (the donor) and a neighboring molecule in the ground state (the acceptor) [36, 37, 38]. The Perrins' model involved a near-field energy of interaction between the oscillating dipoles of two molecules. They were correct that the energy transfer involved dipole perturbations. However, their model did not account quantitatively for the energy transfer between identical molecules in solution (for instance they predicted a transfer energy even in the range 100-500nm).

Then Foerster published his first account of nonradiative energy transfer shortly after the Second World War in 1946 [39]. Foerster appreciated that the premise of dipole–dipole interactions was correct. However, he also realized that the condition of resonance is not limited to just one frequency. Molecules in both ground and excited states have distributions of energy values. In solution, these electronic energy levels are significantly broadened, mainly by vibrational and interactions with the surrounding solvent. This energy distribution has a profound effect on the probability per unit time of spectroscopic transitions, as well as on the rate of energy transfer. Because energy must be conserved during the transfer;

therefore, energy can only be exchanged between donor and acceptor states with identical energy differences between their instantaneous initial and final states. However, this resonance condition is distributed over the total overlapping frequency spectra of the donor and acceptor, and this drastically lowers the probability that the resonance condition will be met. Because of this spectral breadth, the energy that can be donated by an excited donor molecule only exactly matches the energy that can be gained by a neighboring acceptor molecule in a small fraction of the time [38].

Another condition for Foerster transfer is that the perturbation between the two molecules is very weak, such that there is no influence on their absorption and emission spectra. The probability that the frequency of the donor exactly matches the frequency of the acceptor is then calculated by integrating the multiplication of the donor's emission spectrum and the acceptor's absorption spectrum over all frequencies where there is an overlap, always requiring the exact resonance condition. This is known as the ''overlap integral''.

The transfer of energy usually takes place within Donor (D) – Acceptor (A) separations of 0.5–10 nm [38]. A Coulombic perturbation between the excited D molecule on the A molecule takes place through space, and this is approximated as an electric dipole–dipole interaction (classically this is an oscillating dipole). If the conditions are properly matched for the system:

1. The spectral overlap between the emission and absorption spectra of D and A is sufficient,
2. The fluorescence quantum yield of D and the absorption coefficient of A are great enough,
3. The two dipoles are close enough.

There is a significant probability that the excitation energy of the donor will be transferred non-radiatively to the acceptor. Equation 3.1.1.1 describes the rate constant of energy transfer between a separate donor–acceptor pair of molecules through a dipole–dipole interaction [39]:

$$K_{et} = \left(\frac{1}{\tau_d}\right)\left(\frac{R_0}{R_{DA}}\right)^n \qquad (3.1.1.1)$$

Where K_{et} is the rate constant for transferring energy from an excited donor molecule to an acceptor molecule a distance R_{DA} away, τ_d is the donor lifetime in the absence of the acceptor. The parameter n depends on the dimensionality of the system and is 2 for a layer to layer interaction, 4 for a dipole-layer interaction and 6 for a dipole-dipole interaction [40]. R_0, called Foerster radius, is defined as the acceptor-donor separation radius for which the transfer rate equals the rate of donor decay in the absence of acceptor. In other words, when the donor and acceptor radius equals the Förster distance, then the transfer efficiency is 50 percent.

The value of R_0 for a singular pair of donor/acceptor molecules in the dipole-dipole interaction can be calculated as:

$$R_0 = \left(\frac{9000\,(\ln 10)\,Q_d K_p^2}{128\,\pi^5 N_A n_D^4}\,I\right)^{1/6} \quad (3.1.1.2)$$

Where NA is the Avogadro number, n_D the refractive index of the medium, Q_d the quantum yield PL of the donor, K_p^2 is the relative orientation of the donor and acceptor dipoles and I is the integral overlap previously mentioned. K_p^2 is equal to:

$$\kappa^2 = \{2\cos\theta_D\,\hat{r}_{DA}\cdot\hat{p}_A + \sin\theta_D\,\hat{\theta}_D\cdot\hat{p}_A\}^2 \quad (3.1.1.3)$$

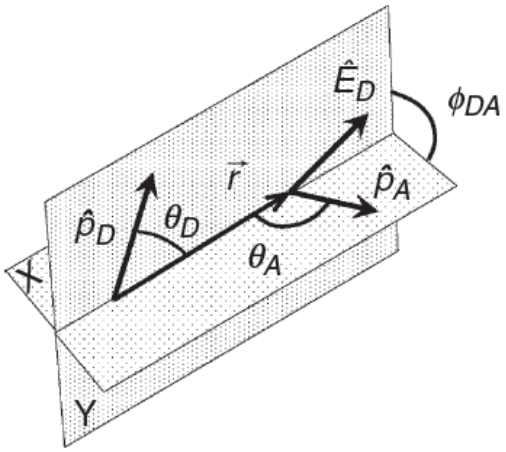

Fig. 3.1.2 The relative orientation of a donor and acceptor dipole [38]

This parameter can range from 0 to 4 but because the randomly orientation between donor and acceptor is usually taken as 2/3.

The energy transfer process can so be envisioned as absorption by the acceptor of the near-field time-dependent electric field disturbance by a classically oscillating electric dipole of the donor

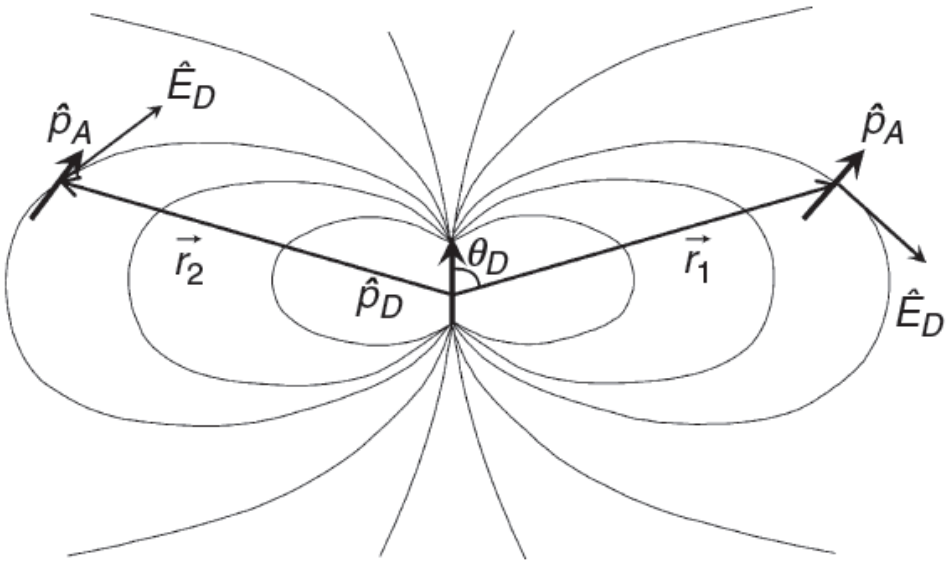

Fig. 3.1.3 Spatial variation of the electric near-field of a classical oscillating dipole. This also represents the correct near-field perturbation between two transition dipoles in a quantum mechanical derivation of RET [38].

The efficiency of energy transfer is a strong function of the separation distance between donor and acceptor (r) and the dimensionality of the system (n) according to the following equation, where R_0 is the Foerster radius:

$$\eta = \frac{1}{1+\left(\frac{r}{R0}\right)^n} \qquad (3.1.1.4)$$

3.1.2 Atomic force microscopy

Atomic force microscopy provides a 3D profile of the surface on a nanoscale, by measuring forces between a sharp probe and surface at very short distance. The probe is supported on a flexible cantilever. The AFM tip "gently touches" the surface and records the small force between the probe and the surface.

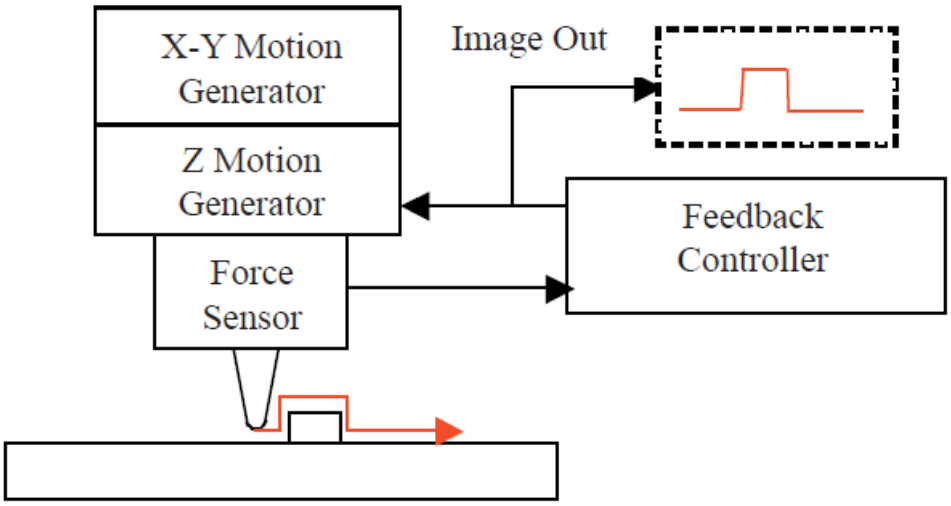

Fig. 3.2.1 Schematis of an AFM

In 1929 Schmalz invented a profiler that utilized an optical lever arm to monitor the motion of a sharp probe mounted at the end of a cantilever. A magnified profile of the surface was generated by recording the motion of the stylus on photographic paper. This type of "microscope" generated profile "images" with a magnification of greater than 1000X. A common problem with stylus profilers was the possible bending of the probe from collisions with surface features. This problem was first addressed by Becker[42] in 1950

and later by Lee [43]. Both Becker and Lee suggested oscillating the probe from a null position above the surface to contact with the surface. In 1971 Russell Young [44] demonstrated a non-contact type of stylus profiler. In his profiler, called the topographiner, Young used the fact that the electron field emission current between a sharp metal probe and a surface is very dependent on the probe sample distance for electrically conductive samples. In the topographiner the probe was mounted directly on a piezoelectric ceramic used to move the probe in a vertical direction above the surface. An electronic feedback circuit monitoring the electron emission was then used to drive the piezoceramic and thus keep the probe sample spacing fixed. In 1981 researchers at IBM were able to utilize the methods first demonstrated by Young to create the scanning tunneling microscope (STM). Binnig and Rohrer [45] demonstrated that by controlling the vibrations of an instrument very similar to Young's topographiner, it was possible to monitor the electron tunneling current between a sharp probe and a sample. The results were astounding. Binnig and Rohrer were able to see individual silicon atoms on a surface [46]. Although the STM was considered a fundamental advancement for scientific research, it had limited applications, because it worked only on electrically conductive samples [47]. A major advancement in profilers occurred in 1986 when Binnig and Quate [48] demonstrated the Atomic Force Microscope. Using an ultra-small probe tip at the end of a cantilever, the atomic force microscope could achieve extremely high

resolutions. In their paper, Binnig and Quate proposed that the AFM could be improved by vibrating the cantilever above the surface.

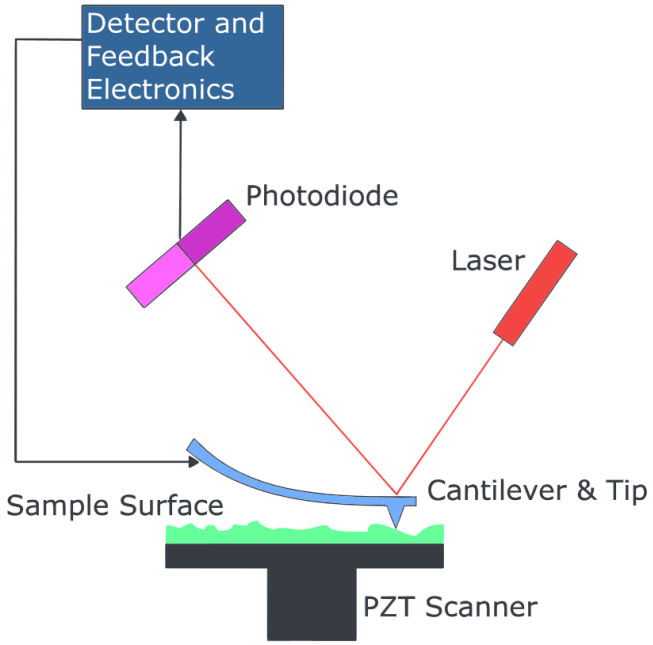

Fig. 3.2.2 Schematic of the first AFM. The feedback is provided by the laser's deflection as consequent of the topography of the sample's surface and flection of the tip [79]

Although the schematic of Fig. 3.2.2 is perhaps still the most iconographic of all AFM machines, today AFM can operate following different principles. For instance our AFM equipment uses piezoelectric technology to generate the feedback. Moreover different imaging techniques are now available on the market:

1. Contact Mode AFM. When the spring constant of cantilever is less than surface interaction, the cantilever bends. The force on the tip is repulsive. By maintaining a constant cantilever deflection (using the feedback loops) the force between the probe and the sample remains constant and an image of the surface is obtained. Provides a fast

scanning, good for rough samples and is used in friction analysis. However not indicated for soft samples.

2. Intermittent Mode (or Tapping mode). The imaging is similar to contact. However, in this mode the cantilever is oscillated at its resonant frequency. The probe lightly "taps" on the sample surface during scanning, contacting the surface at the bottom of its swing. By maintaining a constant oscillation amplitude a constant tip-sample interaction is maintained and an image of the surface is obtained. Allows high resolution of samples that are easily damaged and/or loosely held to a surface. Good for biological samples, but is more challenging to use to image in liquids and has slower scan speeds.
3. Non-contact Mode. The probe does not touch the sample surface, but oscillates above the adsorbed fluid layer on the surface during scanning often used to improve resolution. Because very low force exert on the sample, has an extended probe lifetime that however comes with generally lower resolution. Usually need ultra-high vacuum (UHV) should be used to have best imaging

The AFM equipment used in this work is a tapping mode AFM machine. The dynamics of the motion of a tapping mode AFM tip can be approximate as:

$$m\ddot{z} = -k_c z - \frac{m\omega_0}{Q}\dot{z} + F_{ts} + F_0 cos(\omega t) \qquad (3.1.2.1)$$

where Q, k_c , and ω_0 are the quality factor, spring constant, and angular resonance frequency of the free cantilever, respectively. F_0 and ω are the amplitude and angular frequency of the driving force. M is the effective mass of the tip ($k_c/(2\pi f0)\text{^}2$). F_{ts} are the tip surface interactions (Van der Waals or Lennad-Jones). This equation has a general solution:

$$z(Zc,t) = z0(Zc) + A(Zc)\cos[\omega t + \varphi(Zc)] \qquad (3.1.2.2)$$

Where z_0, A, and φ are the mean deflection, amplitude, and phase shift of the oscillation, respectively. T is the time.

However for this work some simplifications can be done. In fact in our case, for a tapping mode tip oscillating on the same spot using the phase feedback, we have a self-excited system that is forced, through the oscillator control amplifier, to vibrate with constant amplitude. The feedback loop thus assures that the energy loses (both intrinsic to the cantilever and the tip-surface interaction) are exactly compensated by the excitation dynamically in order to keep the amplitude constant. Under these conditions, we can simplifies the main equation as follow:

$$m\ddot{z} + k_c(z-d) = F_{ts}(z) \qquad (3.1.2.3)$$

Where d is the distance between the tip and the sample's surface at the center of the oscillation. Z is the position of the tip during the oscillation. $F_{ts}(z)$ can be approximated within the range of the small oscillation by the first two terms of the Taylor series. The previous equation became:

$$m\ddot{z} + k_c(z - d) = F_{ts}(\mathrm{d}_0) + (z - d_0)\frac{\partial F_{ts}(d0)}{\partial z} \qquad (3.1.2.4)$$

Where d_0 is the equilibrium point given by the root of:

$$k_c(z - d) = F_{ts}(z) \qquad (3.1.2.5)$$

The solution of this equation is:

$$z(t) = d_0 + A\cos[2\pi(f_0 + \Delta f)t)] \qquad (3.1.2.6)$$

Where f_0 is the free frequency of oscillation of the tip, $\Delta f = \frac{f_0}{2k_c} F_{ts}(z)$ and

$$F_{ts}(z) = \frac{-HR}{6z^2} \quad \text{WdV} \qquad (3.1.2.7a)$$

$$F_{ts}(z) = \frac{12E_0}{d_0}\left[\left(\frac{d_0}{z}\right)^{13} - \left(\frac{d_0}{z}\right)^{7}\right] \quad \text{LJ} \qquad (3.1.2.7b)$$

This equations that drive the motion of AFM tipping mode tip on the same spot on the sample's surface will be later used for modeling the RET distance dependence experiment.

3.2 Methodology

To detect the resonance energy transfer we studied the time resolved fluorescence dynamics of the donor for different separation distances between the pair donor/acceptor. The laser excitation at 786nm, provided by the Chameleon, was doubled at 393nm using a BBO crystal and then coupled in an optical fiber connected to an inverted microscope. Here a 100x objective (with a spot size or roughly 800nm) excited the sample and a SNOM tip collected the signal that was then brought to an avalanche photodiode connected to a time correlated photon counting unit to generate the time decays curves. When RET took place we could detected the different slopes in the time decay curves, evidences of a shorter donor exciton lifetime due the extra decay channel provided by the resonance energy transfer.

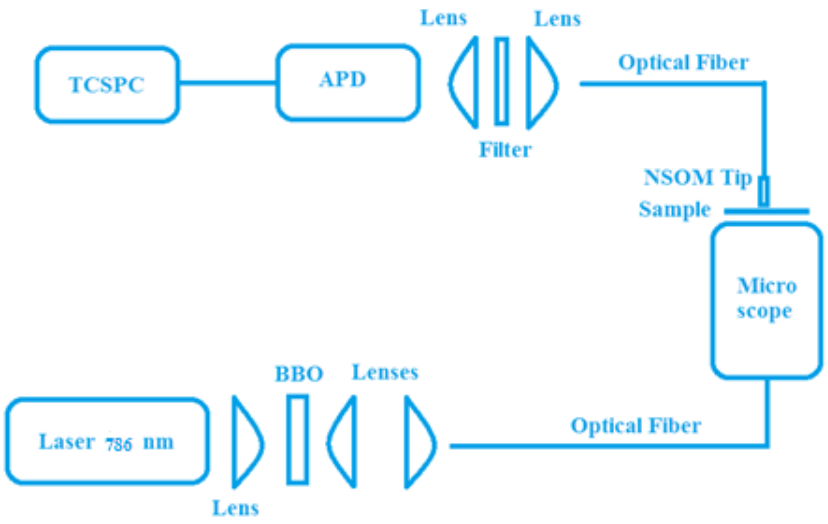

Fig. 3.2.1 Setup schematic

The donor was spincoated as a thin film over a glass microscope slide, and the SNOM tip was coated with the NRs acceptors in an immersion bath using the AFM equipment to avoid damaging the SNOM tip in the process.

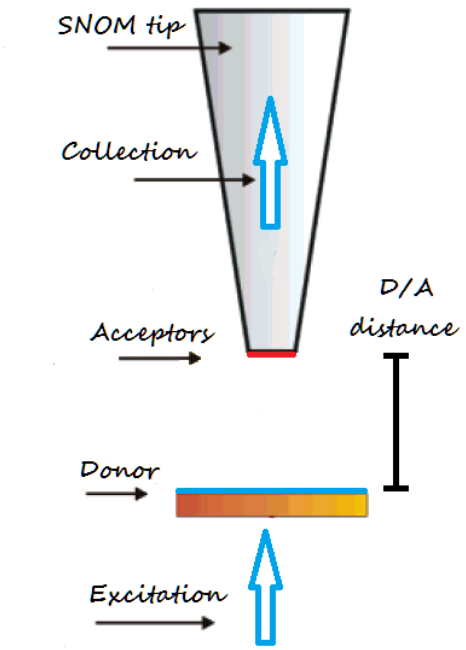

Fig 3.2.2 Experiment schematic

The decay of the donor in absence of any acceptor was taken as reference. Then we studied the decay of the donor in presence of the acceptor for different separation distances, using the AFM equipment to change the donor acceptor separation distance in controlled step, always maintaining the oscillation's amplitude.

3.2.1 The laser system

The laser system used in this work was a Chameleon Ultra II manufactured by Coherent Inc. It is a Ti:Sa tunable modelock femtosecond laser with a repetition rate of 80 MHz and an emission that ranges from 680nm to 1080 nm. For all the experiments in this work it has been combined with a Barium borate crystal (BBO) in order to double the emission frequency in a process called second harmonic generation, in which photons with the same frequency interacting with a nonlinear material are effectively "combined" to generate new photons with twice the energy, and therefore twice the frequency and half the wavelength of the initial photons. For the work in this chapter the laser emission was set to 786 nm therefore the excitation wavelength of the sample resulted 393nm.

3.2.2 Time correlated single photon counting

The method of TCSPC was used to record fluorescence decay curves. For this purpose an SPC140 photon counting card from Becker&Hickl, an avalanche photodiode (PDM from Micro Photonic Devices) have been used. TCSPC is based on the detection of single photons of a periodic light signal, the measurement of the detection times, and the reconstruction of the waveform from the individual time measurements. TCSPC makes use of the fact that for low-level, high-repetition rate signals the light intensity is usually

low enough that the probability to detect more than one photon in one signal period is negligible. The situation is illustrated in Fig. 3.2.2.1

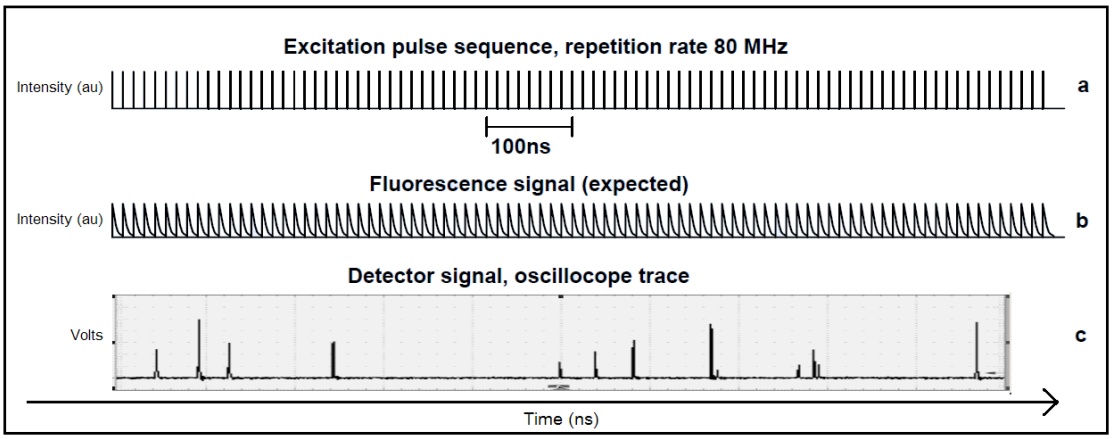

Fig. 3.2.2.1 Detector signal for fluorescence detection [49]

Fluorescence of a sample is excited by a laser of 80 MHz pulse repetition rate (a). The expected fluorescence waveform is (b). However, the detector signal measured by an oscilloscope has no similarity with the expected fluorescence waveform. Instead, it consists of a few pulses randomly spread over the time axis (c). The pulses represent the detection of single photons of the fluorescence signal. Thus, the fluorescence waveform (c) has to be considered a probability distribution of the photons, not anything like a signal waveform. Moreover, Fig. 3.2.2.1 c) shows clearly that the detection of a photon in a particular signal period is a relatively unlikely event. The detection of several photons in one signal period is even less likely. TCSPC therefore neglects the detection of several photons per signal period. The principle is shown in Fig. 3.2.2.2

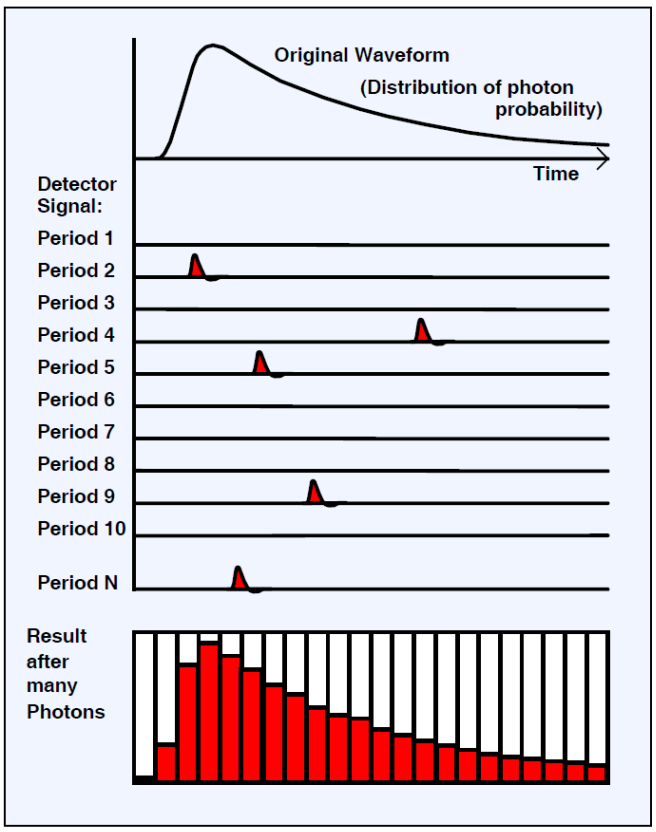

Fig. 3.2.2.2 Principle of TCSPC [49]

As shown above in Fig. 3.2.2.1, the detector signal consists of a train of randomly distributed pulses corresponding to the detection of the individual photons. There are many signal periods without photons, other signal periods contain one photon pulse. When a photon is detected, the arrival time of the corresponding detector pulse in the signal period is measured. The events are collected in a memory by adding a '1' in a memory location with an address proportional to the detection time. After many signal periods a large number of photons has been detected, and the distribution of the photons over the time in the signal period builds up. The result represents the waveform of the optical pulse [49]

3.2.3 The donor acceptor pair

Donor and acceptor have been chosen to satisfy the RET criteria (e.g. maximizing the spectral overlap between the donor emission and the acceptor absorption).

The donor was an American Dye Inc. homopolymer "ADS129BE", Poly[9,9-dioctylfluorenyl-2,7-diyl] - End capped with Dimethylphenyl (DMP) . It shows an absorption maximum at 393 nm and a max photoluminescence on film at 442 nm.

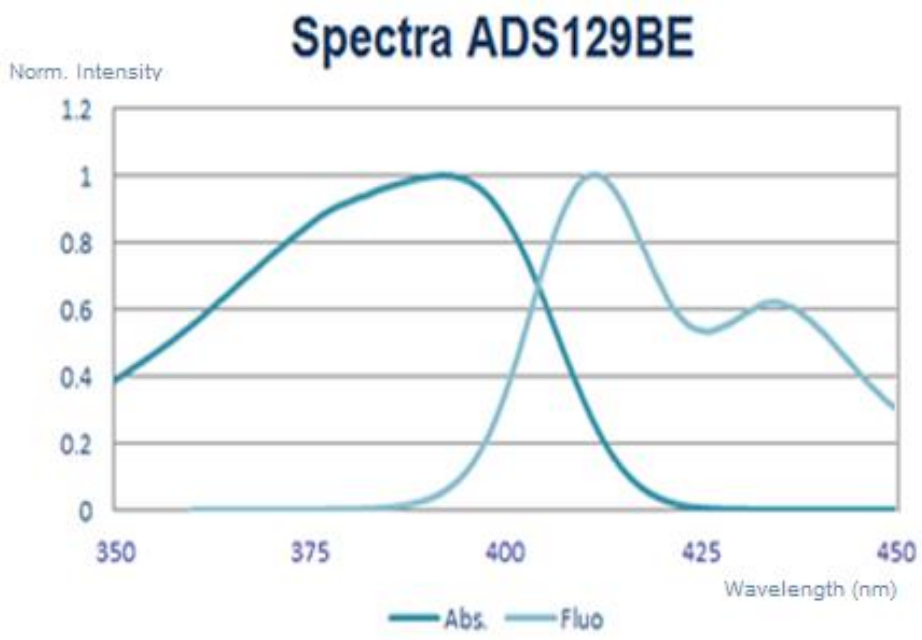

Fig 3.2.3.1 Absorption and emission spectra of the donor [80]

The acceptors were core/shell CdSe/CdS nanorods produced by the Liberato Manna's group in the Italian institute of technology in Genova, synthesized by the seeded-growth approach [33]. They have an average length of roughly 53.8 nm and a diameter of 4.1 nm.

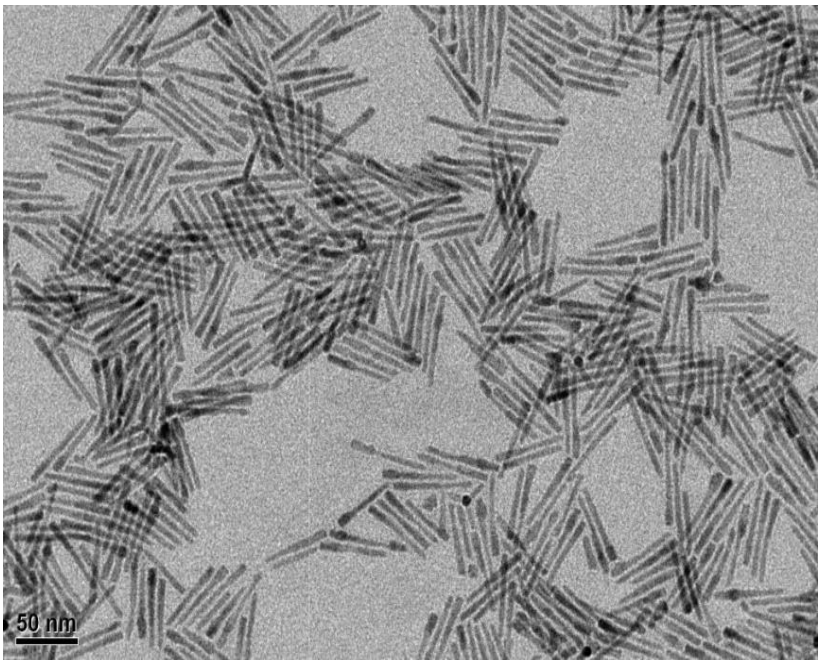

Fig 3.2.3.2 TEM picture of the NRs [33]

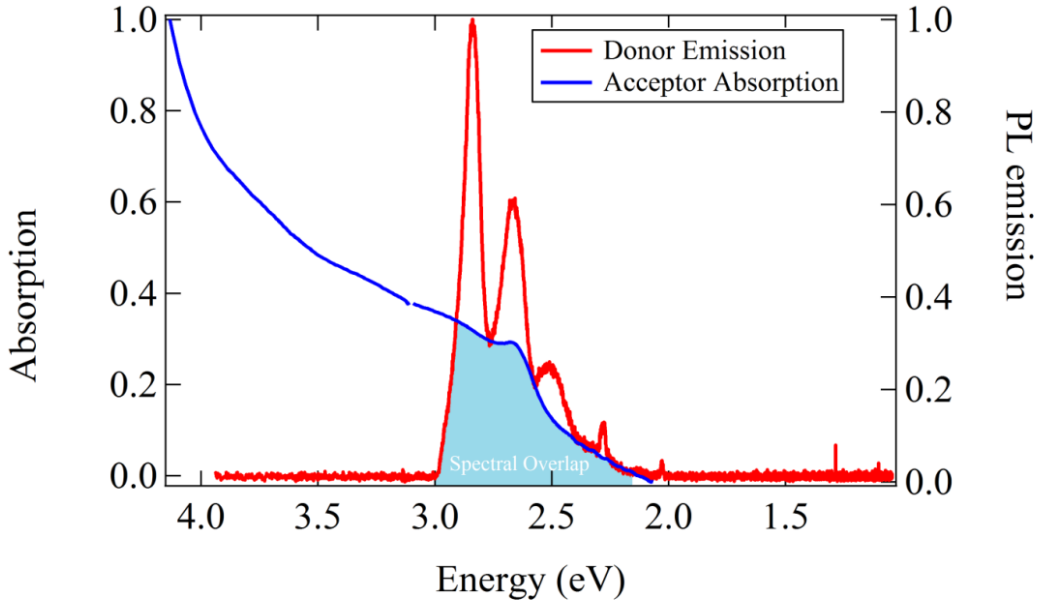

Fig. 3.2.3.3 Spectral overlap between the donor emission and the acceptor absorption.

Both vertical axes are normalized.

3.2.4 The Tip

A very crucial aspect to take in account for this work was the SNOM tip. Typical commercial available SNOM tips were not suitable for our experiment. As is easily notable on fig 3.4.1 those SNOM tip shows a metal ridge all around the aperture. This metal ridge changes slightly dimension from tip to tip and is in the order of hundreds of nm in depth, so way beyond the range of distance where FRET can take place. An average depth for this metal ridge is around 150nm.

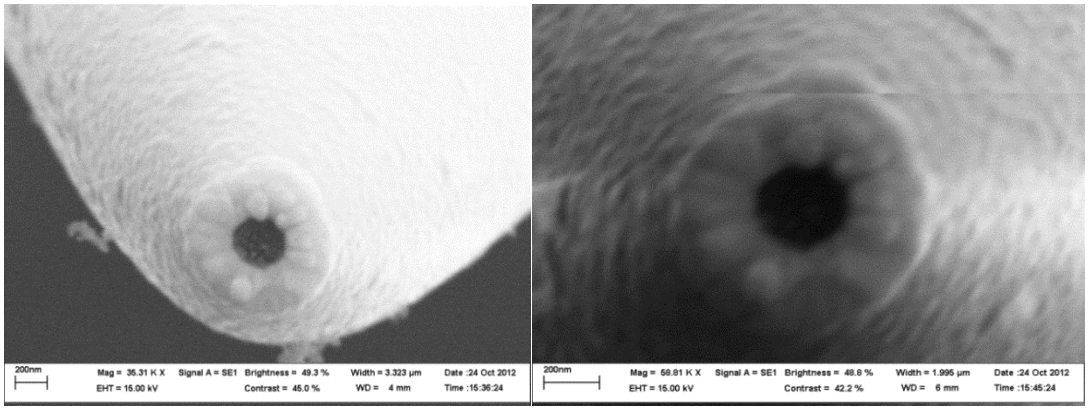

Fig 3.2.4.1 The metal ridge of a commercial SNOM tip

Another unfortunate characteristic of those tips is that they are mounted on a 70 degree angle to the sample's surface. This means that even without the metal ridge, the FRET would occur only in a very small fraction of the aperture and so would be virtually undetectable.

The solution for all this issues was to mill the SNOM tips according our need of a flat smooth surface parallel to the sample using a Focused Ion Beam (FIB)

Polished tips have been bought and milled, in the Mountbatten clean room facility, for this purpose as the follow images shows:

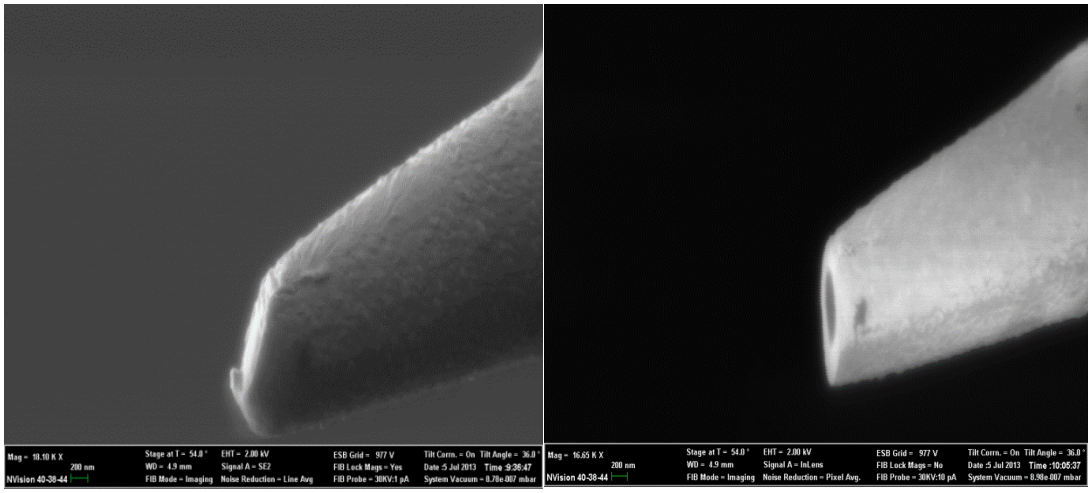

Fig. 3.2.4.2 The tip before and After the FIB cut

On the left picture we can see the tip before the milling. On the right the milled tip with a smooth flat surface that will faces the sample once mounted in our AFM equipment.

3.2.5 Controlling the donor acceptor separation

The AFM/SNOM machine we used for this work is produced by Nanonic Imaging Ltd and is called Multitower 4000. Its capabilities include dry and wet AFM, SNOM, ion conductivity measurement, nano-printing etc. Like every tuning fork tipping mode AFM oscillates vertically over the sample. What we want to achieve with this machine was to create a controlled offset, smaller than a nanometer, between the bottom part of the tip's oscillation and

the sample's surface, always, for each and every point oscillation, maintaining constant the amplitude of it. The amplitude oscillation is set as small as the mechanical characteristic of the tip allowed us, using the gain and oscillation output control parameters in the lock-in amplifier setting of the machine

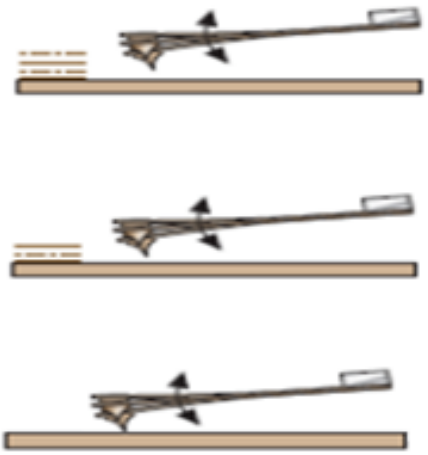

Fig. 3.5.1 Creation of an offset between donor and acceptors

The oscillation's amplitude of the tip is keep constant by the AFM feedback loop. Is imperative, perhaps one of the most important fact to take in account in this work, that the feedback of the AFM must always be active. Only with the feedback active we can be sure that the oscillation's amplitude is always the same for each measurement and, more important perhaps, that the offset we create will be kept constant during the acquisition time of the time decay curves.

To control the donor acceptor separation we used the extra features that, in addition to topographic measurements, the AFM also can provide. For instance can record the amount of force felt by the cantilever as the probe

tip is brought close to the sample surface and then pulled away. This can be used to measure the long range attractive or repulsive forces between the probe tip and the sample surface, elucidating local chemical and mechanical properties like adhesion and elasticity, and even thickness of adsorbed molecular layers or bond rupture lengths. Force curves (force vs. distance curve) typically show the deflection of the free end of the AFM cantilever as the fixed end of the cantilever is brought vertically towards and then away from the sample surface. Experimentally, this is usually done by applying a triangle-wave voltage pattern to the electrodes for the z-axis scanner. This causes the scanner to expand and then contract in the vertical direction, generating relative motion between the cantilever and sample. The deflection of the free end of the cantilever is measured and plotted at many points as the z-axis scanner extends the cantilever towards the surface and then retracts it again.

At this point we have also to recall that the AFM generates its feedback by comparing the signal that continuously received form the tip and an internal electronic reference. This comparison generates an error function that is also generate when a force distance curve is produced. When forcing an oscillatory frequency on the probe, and no other force is applied on the probe (the tip is far from the surface), then the SPM will output a stable signal. The measured signal ("Magnitude" or "Phase") will have a constant value, except for small fluctuations due to noise. This is called the *dynamic value*

because it changes when the probe senses a force. When an external force acts upon the probe (the tip approaches the sample's surface) the phase or amplitude of the oscillating tip, for a particular frequency, will change. Therefore the signal coming into the SPM and processed by the internal lock-in amplifier will have a different value. For this experiment we worked monitoring the phase alteration, and so we work in "Phase feedback", that is the most sensitive feedback for detect external forces.

When, during the tip's approach, there is a certain alternation of the dynamic value then the approach stops and contact is reached. How much of an alternation is determined by us and is called the *set-point*. However the most important parameter is the error, defined as Error = dynamic value – set-point. In phase feedback typically error is set between 0.2 - 0.3 V (Although we work in phase feedback, and so one can expect an error in angle, the AFM provides instead the error in Volts). This means that if the phase was set to be zero then we are going to approach until there is a phase shift of about 0.2V.

When, during the tip approach to the sample's surface, the dynamic value is equal to the set-point then the system turns on the feedback and we are in contact. When in contact the dynamic value is equal to the set-point hence error is zero! After the feedback has been achieved, we decrease the set-point in order to lift the tip in precise steps, creating an offset between the sample's surface and the tip (always maintaining constant the tip

oscillation amplitude). The minimum step in changing the set-point is 0.1 V. To know how many nm correspond a difference of 0.1 V in the set-point once in contact we see the force distance curve.

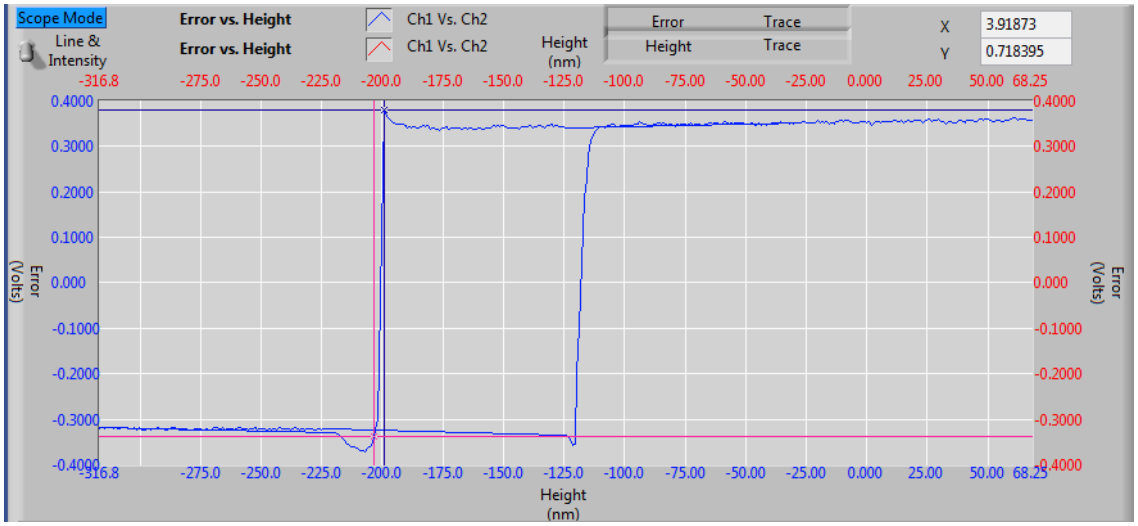

Fig. 3.5.2 The error function that drives the separation distance in a F/D curve

In fig. 3.5.2 we show the force distance curve produced for the experiment described in this chapter. In this curve we can see the tip in free oscillation where no force is felt (extreme right of the curve). Then the piezoelectric sample holder moves toward the tip (left direction of the curve) until finally the tip starts to feel the sample's surface in the point at -200nm on the X axis (the numerical value has relevance only in absolute value) and then reaches the contact with the sample (0V) and retracts. This curve gives us several important information, the first of all being the range, in nm, where we can operate feeling the forces between the tip and sample or, in other words, provides us with a precise range where we can operate without losing the feedback. For example if we would like to create an offset of 10 nm we

already know that will not possible because would not be possible to maintain active the feedback.

Moreover the same graph provides a very precise correlation between the error function and the vertical distance in nm. In this very case every 0.67nm the error function change of 0.1V in the region where the tip feels the force with the sample's surface (feedback active). So if we could first reach the contact, leave the feedback active, and then changing the error function of 0.1V, we could rise the tip of 0.65nm from the sample's surface, having always the oscillation amplitude constant. A precise, controlled offset.

Exactly what we were looking for. A sub-nanometric, precise, reliable technique to control the separation distance in the nanometer regime, creating a specific offset, kept constant increase after increase, as well for the oscillation amplitude, by the feedback loop of the machine. In this way, using this technique, we can really operate every kind of distance dependence experiment without having the necessity of multiple expensive sample and without altering the sample structure or surface.

The only setback using this technique is the limited amount of points that is possible to create adding the offset, limited by the minimum step in the error value change we can create and control (0.1V).

3.3 Results

Now that we know all the theory of the resonance energy transfer, the experimental setup, the equipment, the technique we developed to create the offset needed for the distance dependence, we can finally show the results we obtained:

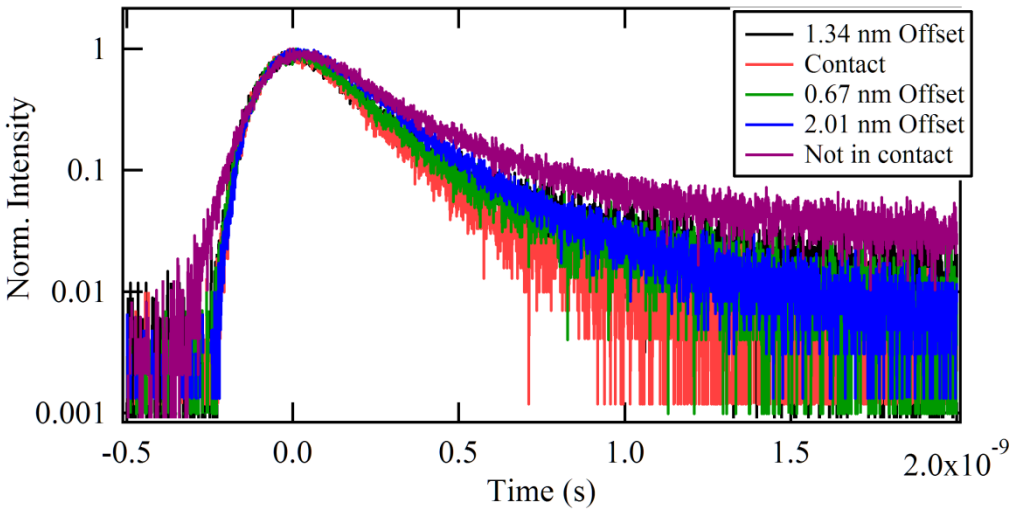

Fig. 3.3.1 Different time decays curve for different position of the tip above the same spot on the sample's surface

Fig 3.3.1 shows the donor's time decay curves for different offsets. The offset ranges from contact (none) to a distance of 2.01 nm away from the sample's surface in steps of 0.67 nm. The tip was always oscillating with the same 10nm amplitude. The measurements were all taken on the same spot, without never losing the feedback. A graph with fewer curves better show how the decay becomes slower lifting away the tip from the sample's surface

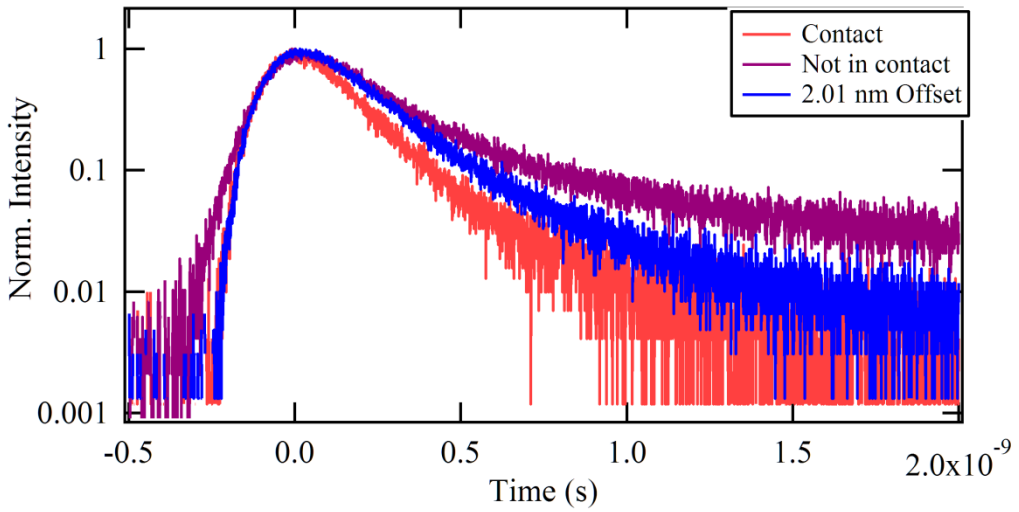

Fig 3.3.2 Different time decays curve for different position of the tip above the same spot on the sample's surface

It is immediately clear how the offset changes the time decay slope, or in other word, the donor exciton lifetime. It is faster in contact, when the tip is at its closest to the sample's surface, and becomes slower offset after offset, lifting the tip away from the sample's surface.

A small difference, in the donor rise time, is also present between contact and not contact state. The rise time is usually defined as the time required for the response to rise from x% to y% of its final value, with 0% to 100% rise time common used for underdamped second order systems, 5% to 95% for critically damped and 10% to 90% for overdamped ones. The rise time of acceptor is equivalent to donor fluorescence lifetime in the presence of an acceptor. The difference in the rise time is mainly explained by the buildup effect for the long acquisition time (more than an hour per point) and the different numerical aperture (NA) of the system at the moment of the data

acquisition (NA being a function of the distance between the tip's aperture and the sample surface. More distant is the tip from the sample's surface bigger is the SNOM NA). In fact, meanwhile all the "feedback active" measurements were taken with virtually the same NA (because the distance between tip and the sample's surface changed of just a couple of nanometers in the extreme case), the reference curve was taken "far away" from the sample's surface (several micrometers away at least), having so a bigger NA and consequentially collecting signal from a much wider and variegated region of the sample's surface.

To fit the decay curves, in order to extract the donor exciton lifetime, a double exponential decays was used. Fig. 3.3.3 show the fast time Tau1 component of the fitting, the time constant related to non-radiative phenomena in the RET

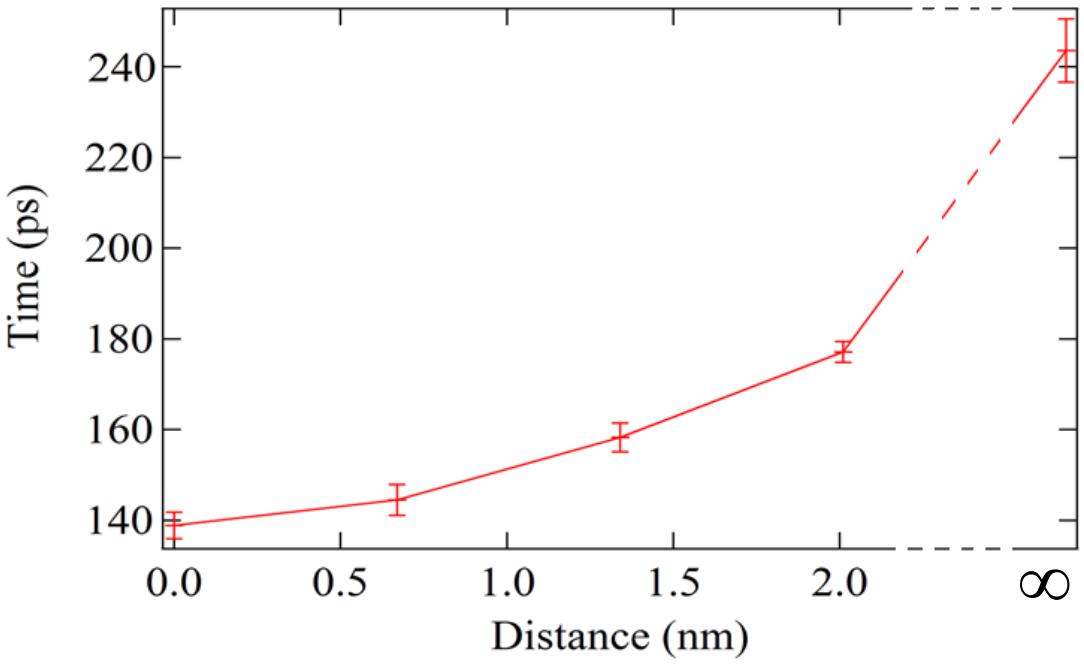

Fig. 3.3.3 Lifetime Vs Offset

Offset (nm)	*Lifetime (pS)*	*Efficiency*
0 (Contact)	*139*	*0.43*
0.67	*144*	*0.40*
1.34	*158*	*0.35*
2.01	*177*	*0.27*
Not in contact	*244*	*0*

Table 3.3.1 Offset Vs Lifetime Vs Efficiency

The experimental data fit extremely well with one particular dimensionality for the resonance energy transfer, the layer to layer interaction of equation (3.1.1.4). This because the dimensionality of the system, where no single molecules interacted but entirely layers.

Forster radius was calculated according equation 3.1.1.4 to be 4.11 nm from the experimental data. This result is very close to the theoretically value of 4.5nm obtained using equation 3.1.1.2.

Moreover we developed a model to calculate the resonance energy transfer efficiencies and the theoretical donor lifetimes as function of the created offset and dimensionality of the system. The model simulates, using equations (3.1.2.1 – 3.1.2.7), the real time sinusoidal behavior of the SNOM tip over the sample's surface and calculates, for each nanosecond, the theoretical value of the RET, integrating then all the values to extract the average RET value efficiency, as function of the offset, for the whole oscillation, using equation 3.3.1:

$$\eta = \frac{1}{2\pi}\int_0^{2\pi} \frac{1}{1+(\frac{Offset+z(t)}{R_0})^n} \qquad (3.3.1)$$

Where *offset* is the offset we introduce changing the set-point, R_0 is the Foerster radius and z(t) is the tip's position over time calculated with eq. 3.1.2.6. Equation 3.1.2.6 also takes into account the oscillation amplitude, the oscillation frequency and the forces acting on the tip as function of the distance between the tip and the sample's surface (Lennard Jones or Van der Waals). The minimum offset has been chosen to be 0.6nm to take into account the presence of the surfactant's thickness of our NR (No RET can take place in the surfactant). In this way we were able to trace, step by step, all the RET dynamic during the tip's oscillation and calculate the efficiency over the oscillation as function of the offset.

The theoretical lifetime in presence of a donor acceptor pair (τ_{DA}) has then been calculated as $\tau_{DA} = \tau_D(1-\eta)$, where τ_D is the donor's lifetime in absence of acceptor and η the efficiency calculated with eq. 3.3.1.

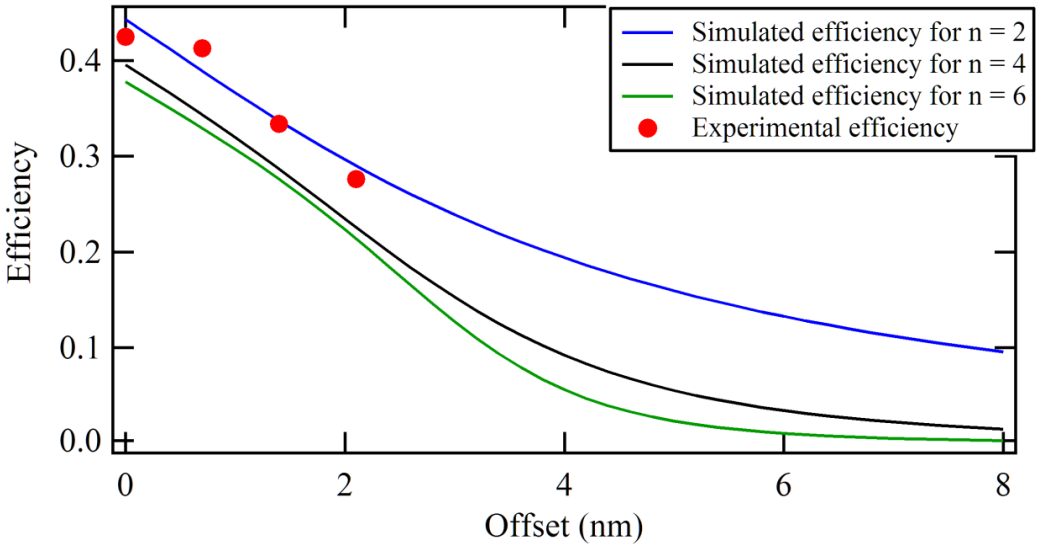

Fig. 3.3.4 Simulated and experimental efficiency vs offset

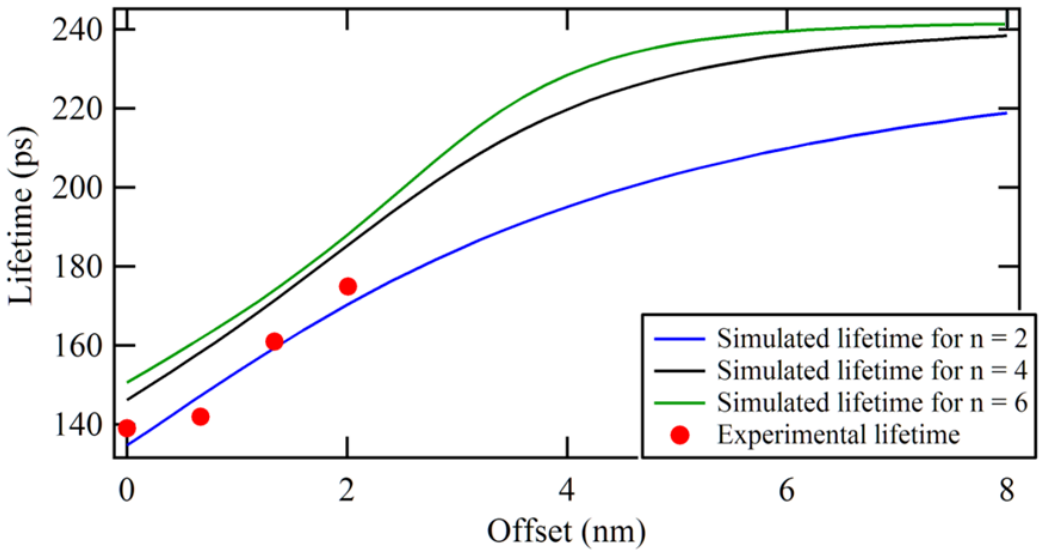

Fig. 3.3.5 Simulated and experimental donor exciton lifetime vs. offset.

Both simulation show an excellent agreement with what found already experimentally for the layer to layer interaction dimensionality of the system.

3.4 Conclusion

We performed an experimental study for the RET distance dependence and established a new non-destructive technique of controlling separation distance in the nanometer regime. The results match with a layer to layer transfer that was expected because the dimensionality of the system and was also confirmed by the theoretical modeling.

We clearly show experimental evidences of resonance energy transfer taking place as function of the donor acceptor separation distance. Results show changes in the donor exciton lifetime that can be explain only by the RET. This energy transfer agrees extremely well with the theoretical prediction for a layer to layer interaction.

Our novel technique allow us for the first time, using an AFM equipment, to investigate RET distance dependence in the range below 10nm with sub-nanometer steps without altering in any way the sample or having the need to mass produce several samples that can be expensive or time consuming. Moreover this technique can be applied for any kind of experiment where very small distance dependence over long time must be observed.

Chapter 4

Nanocrystal lasing

This chapter is dedicated to a different application of nanocrystal: micro-lasers. Two totally different configurations are examined in detail.

The first configuration is based upon an uncoated silica microspheres (used as resonator), an uncoated angle polished fiber (to provide optical excitation to the microsphere), and a coated angle polished fiber used to bring the gain medium (CdSe/CdS NRs) close enough to the resonator in order to obtain lasing. The uncoated end of this fiber was also used to forward the system's emission to the detection system. The system was able to produce lasing working at room temperature, coupling the nanocrystals emission with the whispering gallery mode of the microsphere.

The second configuration uses instead CsSe quantum dots as gain medium and a photonic crystal SiN L3 nanocavity as resonator chamber. Laser regime is once more obtained at room temperature.

4.1 Colloidal NCs microsphere laser

4.1.1 Introduction

In the last years, there has been a wide range of applications for whispering gallery mode resonators. From optical signal processing [50] to bio-sensing [51] pure microspheres made from SiO_2 silica or doped microspheres have been used. At the same time the research of semiconductor nanocrystals lasers has experienced significant growth over the past decade [52, 53]. Recently a "Single-mode tunable laser emission in the single-exciton regime from colloidal nanocrystals", has been published [54]. Unfortunately, coating the silica microsphere with any kind of nanoparticle decreases dramatically the quality factor of the sphere. Moreover once the sphere is coated, only small tunability in the lasing emission is possible. Our aim was to get lasing using a configuration like ref. 54 but avoiding the coating process to achieve a configuration described in ref. [17], using an angled polished fiber instead of a tapered fiber to provide excitation.

4.1.2 Theoretical background

4.1.2.1 Whispering gallery mode resonators

Whispery gallery mode (WGM) resonators consist of a dielectric material, such as silicon dioxide, with spheroidal shape [55]. The high refractive index difference between the dielectric material and the surrounding material (e.g. air), creates an interface where light rays intersect repeatedly with the critical angle, undergoing total internal reflection [56]. In the case that this ray propagates near the surface of the spheres (with radius R) and one round trip is equal to an integer number of wavelength, the constructive interference occurs with resonance condition $x = \frac{2\pi R}{\lambda}$, were λ is the light's wavelength. Therefore, WGM resonators enable optical amplifications and select specific frequencies of light that can be coupled into the optical guides [56]. This type of resonators exhibits high wavelength selectivity and small mode volume that is critical for the development of photonic circuits.

WGMs are characterized by three mode number *n*, *l*, *m* that corresponds to radial, polar and azimuthal components of the electromagnetic field distribution (Fig. 4.1.2.1.1) [57]. More specifically the *n* mode takes values 1, 2, 3… and describes the field intensity distribution in the radial direction. The mode number *l* takes values $l=n-1$ and describes the field intensity distribution in the polar direction. Finally, the mode number

m can take values from *–l* to *l* and indicates the number of maxima in the sinusoidal variation of the field intensity in the equatorial or azimuthal variation.

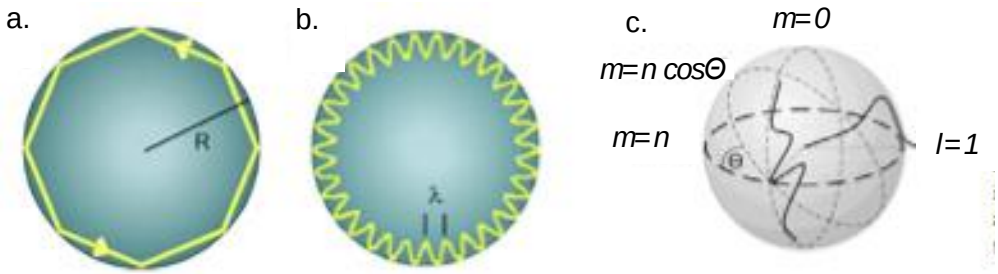

Figure 4.1.2.1.1 Light confinement inside a whispery gallery mode resonator, in (a) geometrical, (b) wave optics approach. (c) Schematic of a spherical micro-cavity showing distribution and spatial orientation of the modes [56]

Some important parameters that characterize a micro-resonator are the quality factor of the cavity (Q-factor), the free spectra range (FSR) and the finesse (F). The Q-factor in an optical resonator indicates the capacity of the resonator to circulate and store light. It is defined as the ratio of stored energy to the energy dissipated to the cycle. The Q-factor is also a measure of energy losses and is defined as the time average energy in the cavity divided by the energy loss per cycle and is given by:

$$Q = \omega_o \frac{Stored\ energy}{Power\ loss} = \omega_o \tau_P \qquad (4.1.2.1.1)$$

where τ_P is a time constant describing the build up or the decay time of stored energy in the cavity, and ω_o is the angular frequency [56]. The space between successive polar modes is defined by the free spectral range (FSR) and is given by the equation:

$$FSR(\Delta\nu_{FSR}) = \frac{c}{2\pi R n_1} \text{ (Hz)} \qquad (4.1.2.1.2)$$

where c is the speed of light, R the resonator radius and n_1 is the effective refractive index of the medium inside the resonator. The finesse factor provides a measure of the filtering properties of the cavity and relates the free spectral range to the resonance linewidth by:

$$F = 2\pi \frac{FSR}{\delta\omega} = 2\pi Q \frac{FSR}{\omega_o} \qquad (4.1.2.1.3)$$

The finesse of an optical resonator can also be defined as the ratio between the free spectral range and its bandwidth and is independent of the resonator length.

4.1.2.2 Angled polished fiber

The main idea of an angled polished fiber is illustrated in Fig. 4.1.2.2.1

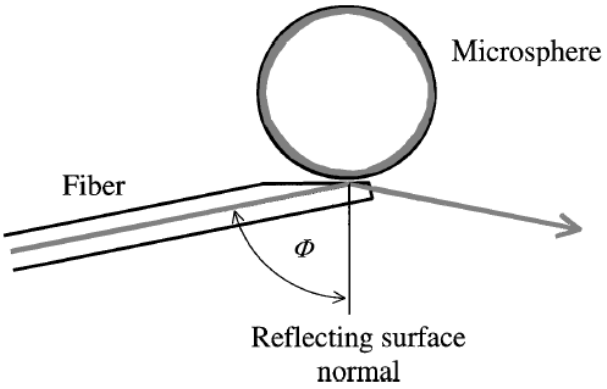

Fig. 4.1.2.2.1 Angle-polished fiber coupler for WG modes [58].

The tip of a single-mode fiber (SMF) is angle cleaved with a steep angle. When it is incident upon the angled surface, the light propagating inside the core undergoes total internal ref lection and escapes the fiber. With the sphere positioned in the range of the evanescent field from the core area, an efficient energy exchange occurs at resonance between the waveguide mode of the SMF and the WG mode in the sphere. The angle of the polish is chosen to fulfill the phase-matching requirement $\varphi = \arcsin (n_{sphere} / n_{fiber})$, where n_{sphere} is the effective refractive index for azimuthal propagation of the WG modes (as closed waves circulating in the sphere) and n_{fiber} is the effective refractive index for the guided wave in the fiber. Since the linear dimensions of the angle-cut core of the SMF match the scale of the evanescent field overlap area the system is equivalent to a prism coupler with the focusing optics eliminated [58].

4.1.3 Methodology

The setup used for the experiment described in this section is illustrated in fig. 4.1.3.1:

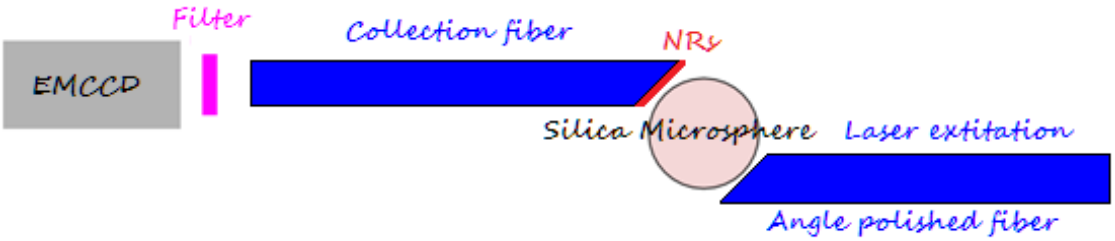

Fig. 4.1.3.1 NRs WGM lasing setup

An angle polished fiber was used to excite whispering gallery mode in the microsphere. A second fiber, with NRs coating one end, was carefully brought in proximity of the microsphere (always avoiding physical contact between the fiber and the microsphere). When close enough to the microsphere, the NRs emission was checked using an EMCCD camera, working in EM mode, to see if the emission of the NRs was enhanced enough by the microsphere resonator to produce lasing.

The NRs used as gain medium were the same of the previous chapter. The excitation was provided by the same laser described in section 3.2.1. The signal at 800nm of the chameleon ultra II was doubled via a BBO crystal and the signal coupled into the angle polished fiber with a coupling ratio of 32%. The fiber, held on a piezoelectric translation stage, was a single mode fiber cleaved using a $C0_2$ laser based fiber cleaver produce by Optek. The NRs

were deposited on the fiber's end by immersion, and the fiber held by a Thor labs piezoelectric translation stage with a step resolution of 20nm.

EMCCD cameras overcome a fundamental physical constraint to deliver high sensitivity with high speed. Traditional CCD cameras offered high sensitivity but at the expense of slow readout. Hence they were often referred to as 'slow scan' cameras. The fundamental constraint came from the CCD charge amplifier. To have high speed operation the bandwidth of the charge amplifier needs to be as wide as possible but it is a fundamental principle that the noise scales with the bandwidth of the amplifier hence higher speed amplifiers have higher noise. Slow scan CCD's have relatively low bandwidth and hence can only be read out at modest speeds typically less than 1MHz. EMCCD cameras avoid this constraint by amplifying the charge signal before the charge amplifier and hence maintain unprecedented sensitivity at high speeds. By amplifying the signal the readout noise is effectively by-passed and readout noise no longer is a limit on sensitivity.

A CCD camera mounted on a moving bracket provided visual feedback for the microsphere and the fiber.

The microsphere used was produced by CO_2 laser thermal processing of fiber tapers to which they remained attached after the completion of the fabrication process. It had a diameter of 60 μm

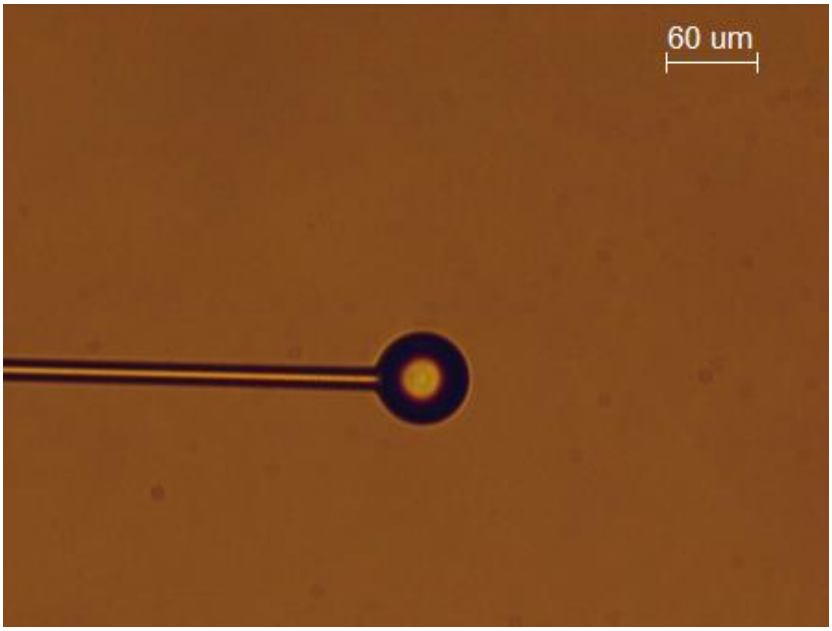

Fig. 4.1.3.2 The silica microsphere

4.1.4 The results

Using the methodology described in the previous section, working with extremely caution and patience to avoid contact between the coated fiber and the microsphere, thanks to the extreme sensitivity of our EMCCD, was possible to acquire the spectra showed in fig. 4.1.4.1:

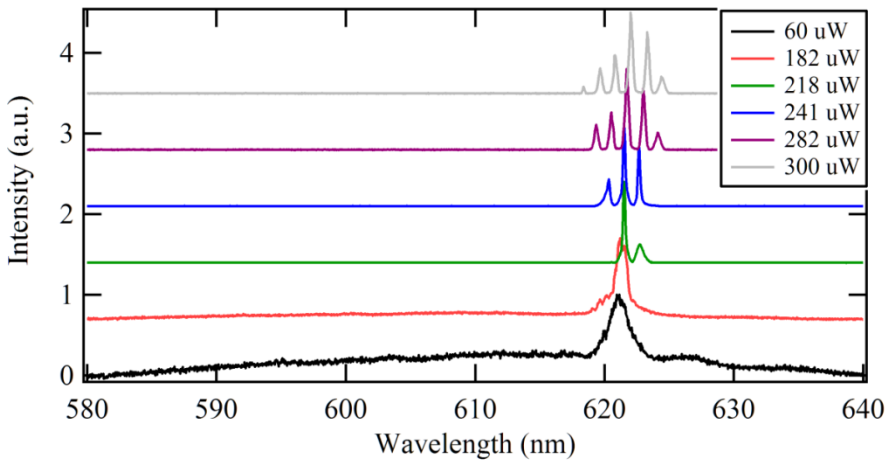

Fig. 4.1.4.1 NRs multimode lasing emission from the system

In this graphs is possible to clearly appreciate how, increasing the pump power for a given fiber/microsphere position, an enhancement in the PL emission spectrum of the NRs appears when the pump power of the uncoated angle polished fiber reaches 60μW. Moreover increasing even further the pump power, we can observe the linewidth emission of the central peak shrinking (typical evidence for lasing regime) and the appearing of more lasing modes.

Fitting the central peak we obtain the values showed in the next graph:

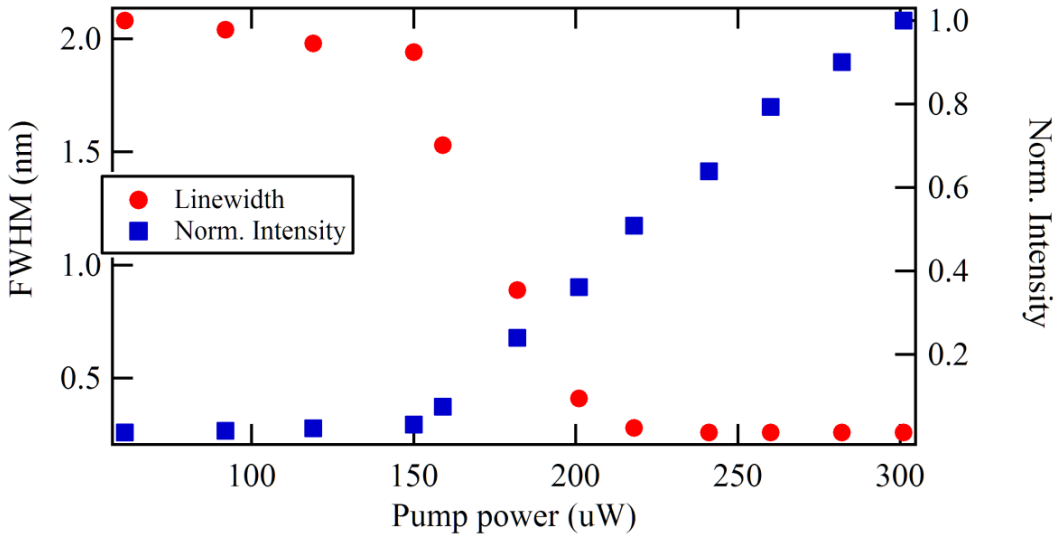

Fig. 4.1.4.2 Linewidth vs. norm. Lasing intensity vs. pump power

In fig. 4.1.4.2 is possible to see all the evidences of lasing regime. The emission linewidth narrows dramatically of one order of magnitude from

2nm to 0.26 nm. The NRs PL emission intensity shows nonlinear increasing typical of lasing regime, with a threshold, calculated as function of the pumping power that excites the silica microsphere, of roughly 145μW. Moreover the free spectral range, calculated as the main inter-peaks distance, is roughly 1.43nm, and is very close to the theoretical of 1.41nm calculated.

4.1.5 Conclusion

The results showed in fig. 4.1.4.2 clearly have all the characteristics of lasing behavior, leaving very little room for doubts. Lasing regime was achieved and the main idea behind this experiment has been proved correct and successfully. We made a point!!! As further confirmation that the lasing was taking place not because some contamination of NRs on the microsphere surface, after every run a clean fiber was put in place of the coated fiber, without changing the excitation alignment, and the EMCCD signal was every time recorded without never show PL emission in the NRs range.

Unfortunately unpleasant circumstances, which did not depend by the author, made impossible further experiments and more precise measurements, like a lasing distance dependence (between the fiber and the microsphere) or an estimation of the number of the NRs involved in the lasing regime. However, taking into account the extreme dilution of the NRs solution used

for coating the tip, the few hundreds micrometer spatial range where the NRs could couple to the microsphere (ref. 17), and following the equation in section 4.2 of ref. 18, we can assume, without being too wrong, that only an handful of NRs per mode (most likely even fewer then ref. 18) were involved in the lasing regime. Unfortunately the collected data lack the necessary parameters that could allow us a more rigid estimation.

4.2 Lasing from CdSe QDs embedded in a SiN L3 nanocavity

4.2.1 Introduction

Two-dimensional photonic crystal (2D PC) nano-cavities are optical structures that confine light into a mode volume. Such confinement makes them attractive systems to explore a range of fundamental phenomena such as the Purcell effect, ultralow threshold lasers [60], and optical nonlinear effects. Up to now, most progress using nanocavities to manipulate light–matter interactions has concentrated on fabricating structures based on III-V semiconductors. Such compound semiconductors have a large refractive index, which makes them a favorable system to efficiently confine light in

three dimensions. However, excitonic emission from III-V semiconductors can only be generated at cryogenic temperatures, with emission limited to near infrared wavelengths.

There is, however, growing interest in the development of nanocavity systems that work at visible wavelengths where emission is generated from organic molecules, conjugated polymers, or inorganic nanocrystals. Recently, silicon nitride (SiN) has emerged as a promising material system for optoelectronic and photonic applications, with photoluminescence and electroluminescence generated at visible wavelengths at room temperature. Importantly, SiN has a refractive index in the range 2 to 2.5, suggesting that a hexagonal 2D PC based on SiN can support a full TE-like bandgap of width more than 70 nm at visible wavelengths [61].

4.2.2 Theoretical background

In spite of the fact that PCs have attracted high attention only during the last several decades, first assumptions of possibility to control the light propagation using the periodic structures relate to 1887 [61]. Almost after 100 years in 1972, Soviet Union scientist V.P. Bykov published a paper where he described the possibility to use periodic structures for the spontaneous emission control [63]. However, the first works assumed to start the intensive progress of PC are the works of E.Yablonovitch and S. John

which was issued in 1987 [64, 65]. Papers are dedicated to the possibility of spontaneous emission management as well as the possibility of the radiation propagation control using periodic structures. In 1990, K.M. Ho, C.T. Chan and C.M. Soukoulis [66] obtained the band structure of the PC with FCC lattices (opal structure) which consisted of dielectric spheres with high refractive index placed in air. In 1992, H.S. Sozuer and J.W. Haus [67] computed the band structure of the PC with inverted FCC lattice (also known as inverted opal). The term inverted opal means that instead of dielectric spheres placed in air, the inverted FCC lattice consists of a number of spherical cavities separated by baffles with higher refractive index. In 2000, the first 3D PC which had the complete PBG within near infrared range was obtained [68, 69]. Since then the researched in the PC area booming.

A photonic crystal corresponds to a periodic dielectric function $\varepsilon(\vec{x}) = \varepsilon(\vec{x} + \vec{R}_i)$ for some primitive lattice vectors $\vec{R}_i$. In this case, the Bloch–Floquet theorem for periodic eigenproblems states that the solutions to eq 4.2.2.1

$$\vec{\nabla} \times \frac{1}{\varepsilon} \vec{\nabla} \times \vec{H} = \left(\frac{w}{c}\right)^2 \vec{H} \qquad (4.2.2.1)$$

where ε is the dielectric function ε(x, y, z) and c is the speed of light, can be chosen of the form $\vec{H}(\vec{x}) = e^{i\vec{k}\vec{x}}\, \vec{H}_{n\vec{k}}(\vec{x})$ with eigenvalues $w_n(\vec{k})$, where $\vec{H}_{n,\vec{k}}$ is a periodic envelope function satisfying:

$$\overrightarrow{(\vec{\nabla} + i\vec{k})} \times \frac{1}{\varepsilon} \overrightarrow{(\vec{\nabla} + i\vec{k}} \times \vec{H}_{n,\vec{k}} = \left(\frac{w_{n(\vec{k})}}{c}\right)^2 \vec{H}_{n,\vec{k}} \qquad (4.2.2.2)$$

yielding a different Hermitian eigenproblem over the primitive cell of the lattice at each Bloch wavevector $\vec{k}$. This primitive cell is a finite domain if the structure is periodic in all directions, leading to discrete eigenvalues labeled by n = 1,2,3 …. These eigenvalues $w_n(\vec{k})$, are continuous functions of $\vec{k}$, forming discrete "bands" when plotted versus the latter, in a "band structure" or dispersion diagram. Both ω and $\vec{k}$ are conserved quantities, meaning that a band diagram maps out all possible interactions in the system. (Note also that $\vec{k}$ not required to be real; complex $\vec{k}$ gives evanescent modes that can exponentially decay from the boundaries of a finite crystal, but which cannot exist in the bulk). Moreover, the eigensolutions are periodic functions of $\vec{k}$ as well. Thanks to this periodicity, one need only compute the eigensolutions for $\vec{k}$ within the primitive cell of this reciprocal lattice or, more conventionally, one considers the set of inequivalent wavevectors closest to the $\vec{k}$ = 0 origin, a region called the first Brillouin zone. Furthermore, the first Brillouin zone may itself be redundant if the crystal possesses additional symmetries, such as mirror planes, by eliminating these redundant regions, one obtains the irreducible Brillouin zone, a convex polyhedron that can be found tabulated for most crystalline structures[69].

A complete photonic band gap is a range of ω in which there are no propagating (real $\vec{k}$) solutions of equations (4.2.2.1) for any $\vec{k}$, surrounded by propagating states above and below the gap. There are also incomplete gaps,

which only exist over a subset of all possible wavevectors, polarizations, and/or symmetries. onsider a one-dimensional system with uniform $\varepsilon = 1$, which has plane waveeigensolutions $\omega(k) = ck$. This ε has trivial periodicity a for any $a \geq 0$, with $a = 0$ giving the usual unbounded dispersion relation. We are free, however, to label the states in terms of Bloch envelope functions and wavevectors for some $a \neq 0$, in which case the bands for $|k| > \pi/a$ are translated ("folded") into the first Brillouin zone, as shown by the dashed lines in fig. 4.2.2.1(left).

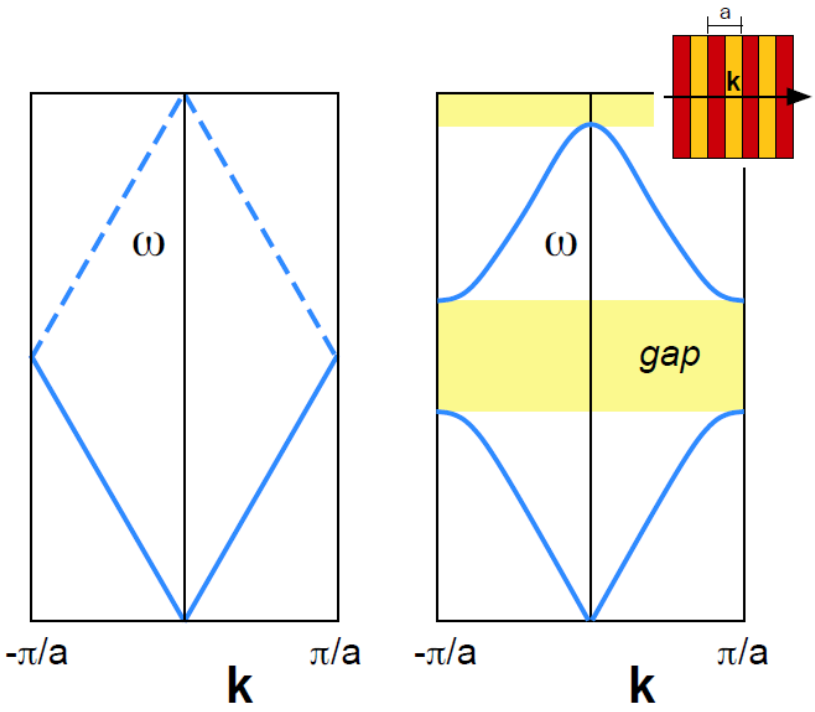

Fig. 4.2.21 Left: Dispersion relation (band diagram), frequency ω versus wavenumber k, of a uniform one-dimensional medium, where the dashed lines show the "folding" effect of applying Bloch's theorem with an artificial period-icity a. Right: Schematic effect on the bands of a physical periodic dielectric variation (inset), where a gap has been opened by splitting the degeneracy at the $k = \pm\pi/a$ Brillouin-zone boundaries (as well as a higher-order gap at $k = 0$) [69].

In particular, the $k = -\pi/a$ mode in this description now lies at an equivalent wavevector to the $k = \pi/a$ mode, and at the same frequency; this accidental degeneracy is an artifact of the "artificial" period we have chosen. Instead of writing these wave solutions with electric fields, we can equivalently write linear combinations $e(x) = \cos(\pi x/a)$ and $o(x) = \sin(\pi x/a)$ as shown in fig. 4.2.2.2, both at $\omega = c\pi/a$.

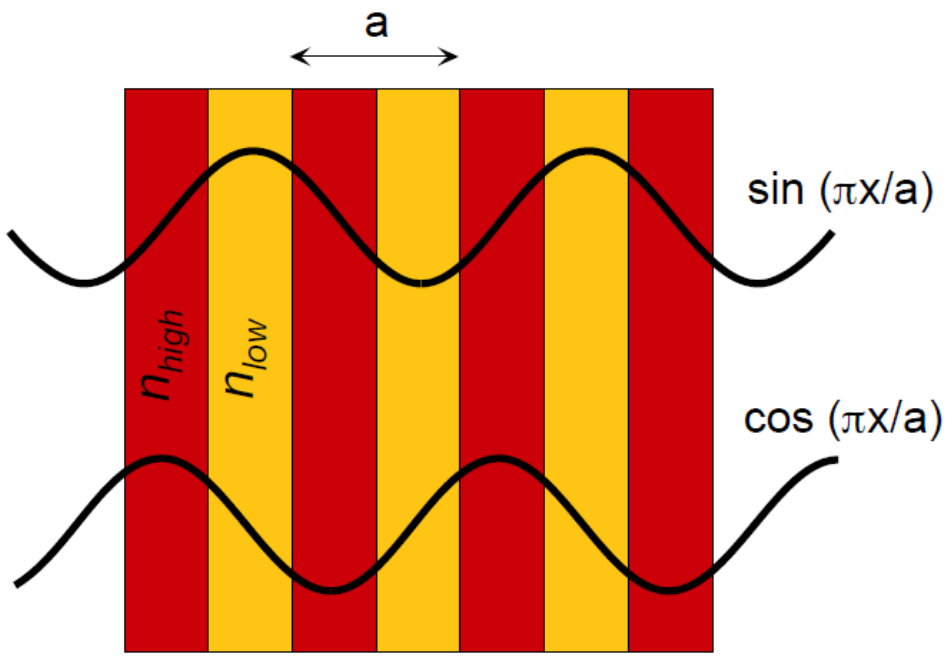

Fig. 4.2.2.2 Schematic origin of the band gap in one dimension. The degenerate $k = \pm\pi/a$ planewaves of a uniform medium are split into $\cos(\pi x/a)$ and $\sin(\pi x/a)$ standing waves by a dielectric periodicity, forming the lower and up-per edges of the band gap, respectively—the former has electric-field peaks in the high dielectric (n-high) and so will lie at a lower frequency than the latter (which peaks in the low dielectric) [69]

Now, however, suppose that we perturb ε so that it is nontrivially periodic with period a; for example, a sinusoid $\varepsilon(x) = 1 + A\cos(2\pi x/a)$, or a square wave as in the inset of fig. 4.2.2.1. In the presence of such an oscillating "potential," the accidental degeneracy between e(x) and o(x) is broken: supposing $A > 0$,

then the field e(x) is more concentrated in the higher-ε regions than o(x), and so lies at a lower frequency. This opposite shifting of the bands creates a band gap, as depicted in fig. 4.2.2.1(right) [69].

By the same arguments, it follows that any periodic dielectric variation in one dimension will lead to a band gap. More generally, it follows immediately from the properties of Hermitian eigensystems that the eigenvalues minimize a variational problem:

$$w^2_{n,\vec{k}} = \min_{\vec{E}_{n,\vec{k}}} \frac{\int \left|(\vec{\nabla}+i\vec{k})\times\vec{E}_{n,\vec{k}}\right|^2}{\int \varepsilon \left|\vec{E}_{n,\vec{k}}\right|^2} c^2 \qquad (4.2.2.3)$$

in terms of the periodic electric field envelope $\vec{E}_{n,\vec{k}}$, where the numerator minimizes the "kinetic energy" and the denominator minimizes the "potential energy." Here, the n > 1 bands are additionally constrained to be orthogonal to the lower bands:

$$\int \vec{H}^*_{m,\vec{k}} \overrightarrow{H}_{n,\vec{k}} = \int \varepsilon \vec{E}^*_{m,\vec{k}} \vec{E}_{n,\vec{k}} = 0 \qquad (4.2.2.4)$$

for m < n. Thus, at each $\vec{k}$, there will be a gap between the lower "dielectric" bands concentrated in the high dielectric (low potential) and the upper "air" bands that are less concentrated in the high dielectric. The air bands are forced out by the orthogonality condition, or otherwise must have fast oscillations that increase their kinetic energy. (The dielectric/air bands are analogous to the valence/conduction bands in a semiconductor) [69].

In order for a complete band gap to arise in two or three dimensions, two additional hurdles must be overcome. First, although in each symmetry direction of the crystal (and each $\vec{k}$, point) there will be a band gap by the one-dimensional argument, these band gaps will not necessarily overlap in frequency (or even lie between the same bands). In order that they overlap, the gaps must be sufficiently large, which implies a minimum ε contrast (typically at least 4/1 in 3d). Since the 1d mid-gap frequency varies inversely with the period a, it is also helpful if the periodicity is nearly the same in different directions thus, the largest gaps typically arise for hexagonal lattices in 2d and fcc lattices in 3d, which have the most nearly circular/spherical Brillouin zones. Second, one must take into account the vectorial boundary conditions on the electric field: moving across a dielectric boundary from ε to some ε' < ε, the inverse "potential" will decrease discontinuously if E is parallel to the interface and will increase discontinuously if E is perpendicular to the interface. This means that, whenever the electric field lines cross a dielectric boundary, it is much harder to strongly contain the field energy within the high dielectric, and the converse is true when the field lines are parallel to a boundary. Thus, in order to obtain a large band gap, a dielectric structure should consist of thin, continuous veins/membranes along which the electric field lines can run this way, the lowest band(s) can be strongly confined, while the up-per bands are forced to a much higher frequency because the thin veins cannot support multiple modes (except for two

orthogonal polarizations). The veins must also run in all directions, so that this confinement can occur for all $\vec{k}$, and polarizations, necessitating a complex topology in the crystal [69].

4.2.3 Methodology

The optical properties of the embedded QDs were investigated using far field optical spectroscopy according the following setup schematic:

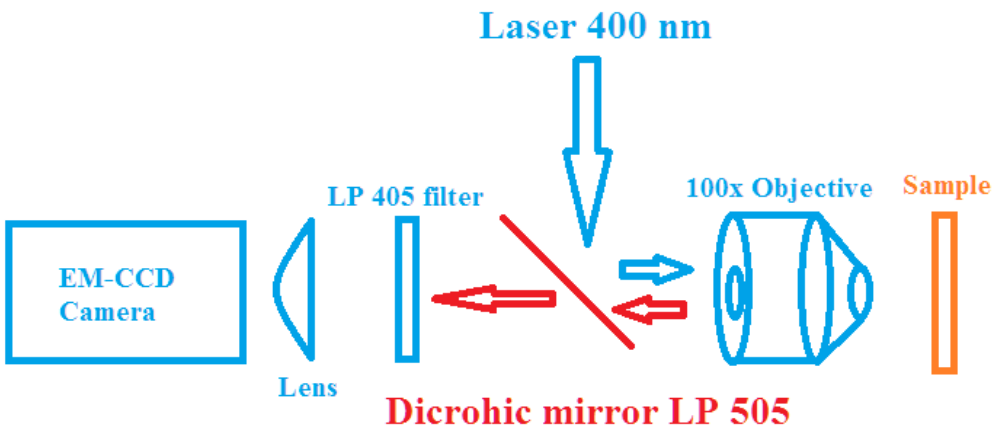

Fig. 4.2.3.1 Setup schematic

The excitation was provided by a Coherent Vitesse 800, with a repetition rate of 80 MHz, doubled via a BBO crystal from 800nm to 400nm. This excitation was focused on the sample via a 100x objective giving a sub micrometric spot size (roughly 800nm). The signal collected was filtered a first time by a long pass 505 nm dichroic mirror, then by a Semrock long pass

405nm filter and then again focused, with a 7.5cm focus lens, in the Andor Newton EMCCD camera working in EM mode.

The slit aperture of the Traix 550 spectrograph, for all the measurements, was 40 microns. To detect the time decays of the QDs, a TCSPC module SPC-140 Becker, with a Photodevice APD, was also used. The sample was mounted on a piezoelectric translation stage with a step resolution of 40 nm.

The nanocavities were fabricated by Prof. David Lidzey group on a pre-etched, freestanding SiN membrane of thickness d=200 nm and refractive index of n=2.1 supplied by Silson Ltd. On the sample a series of 12 regular L3 photonic crystal nanocavities (L3 means line defect on the periodic structure of the sample with 3 holes missing) were written into a 180 nm thick polymethyl methacrylate positive photoresist coated on the SiN membrane using electron beam lithography, having all a lattice constant of a=260 nm and a diameter of D=0.6a, but different side-hole displacements S (Is the horizontal distance between the last hole in line with the L3 cavity and the hole before). This pattern was then transferred into the SiN membrane using a CHF3-based reactive ion etching (RIE) technique. Nano-cavity dimension were roughly 1 micron long and 450 nm wide [70]

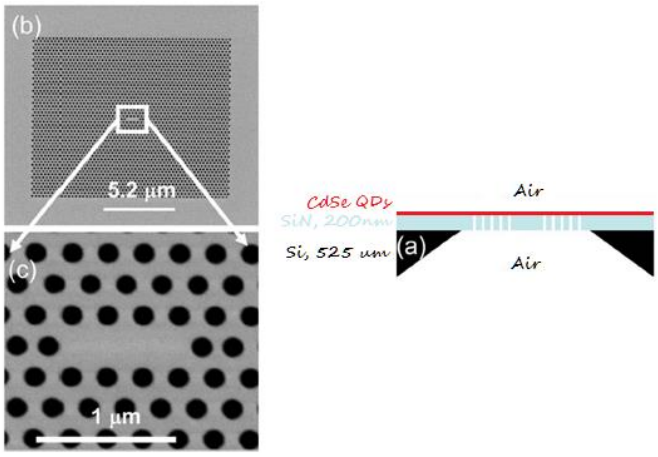

Fig. 4.2.3.2 (a) Schematic of the cavity. (b), (c) Sem image of the PC and nanocvity [70]

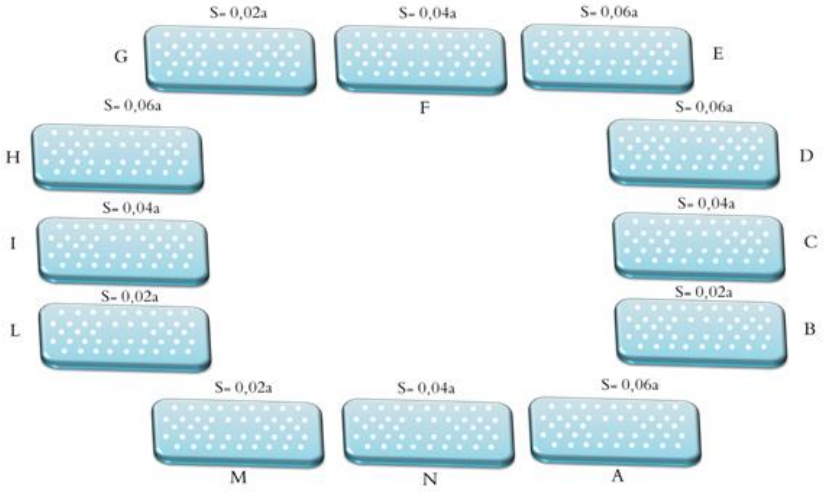

Fig. 4.2.3.3 Samples nomenclature with different S side-hole displacement

Sample	Side-hole displacement (nm)
A	15.6
B	5.2
C	10.4
D	15.6
E	15.6

F	10.4
G	5.2
H	15.6
I	10.4
L	5.2
M	5.2
N	10.4

Table 4.2.3.1 Sample side-hole displacement S

The quantum dots were then randomly spincoated on the samples as gain medium. A power dependence study and a time decay measurement were performed on the QDs PL emission for each individual nanocavity in search of enhancement PL emission and eventually lasing evidence. Not all of them showed a relevant enhancement of the PL emission, nor lasing regime behavior. Except one, with a side-hole displacement of S=0.04a (Sample N)

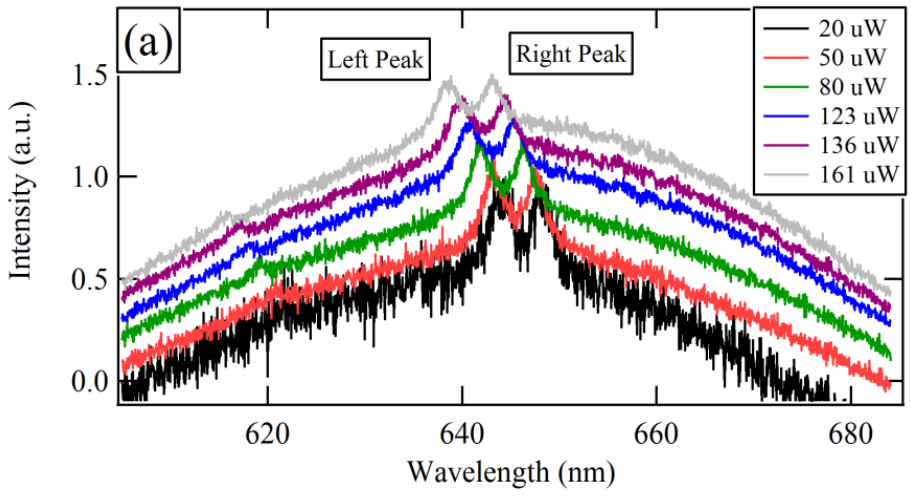

Fig 4.2.3.4 QDs PL typical emission for different pump power from samples.

4.2.4 Results

Fig. 4.2.4.1 shows the enhanced PL spectra of sample N for some different pumping powers.

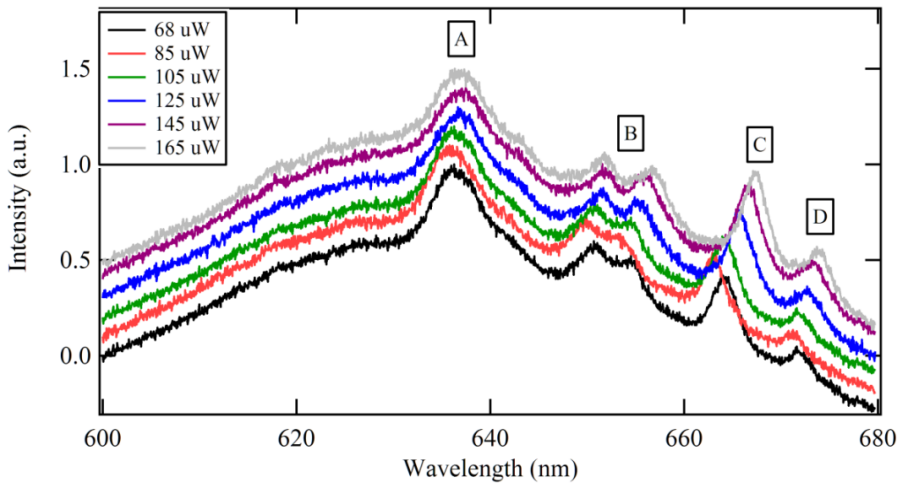

Fig 4.2.4.1 QDs PL emission for different pump power for sample N

Four different enhancement regions/peaks, named A-B-C-D, are evident in this spectrum. Of this four regions only peak C showed lasing behavior. The following graphs show the power dependence, the power-linewidth dependence, the emission shift of the sample to prove lasing behavior:

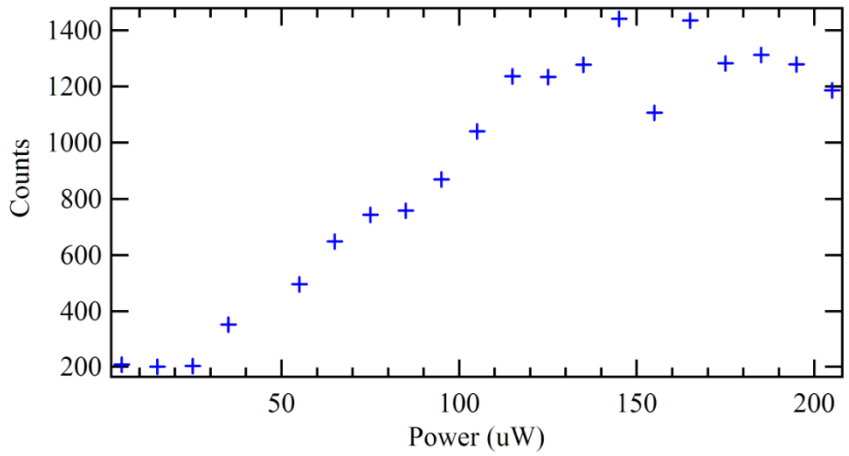

Fig. 4.2.4.2 Power dependence characteristic

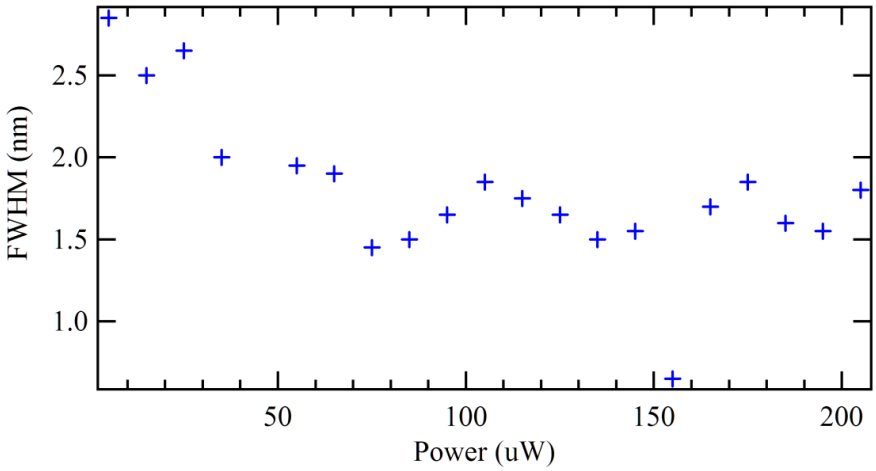

Fig. 4.2.4.3 Pump power vs. FWHM

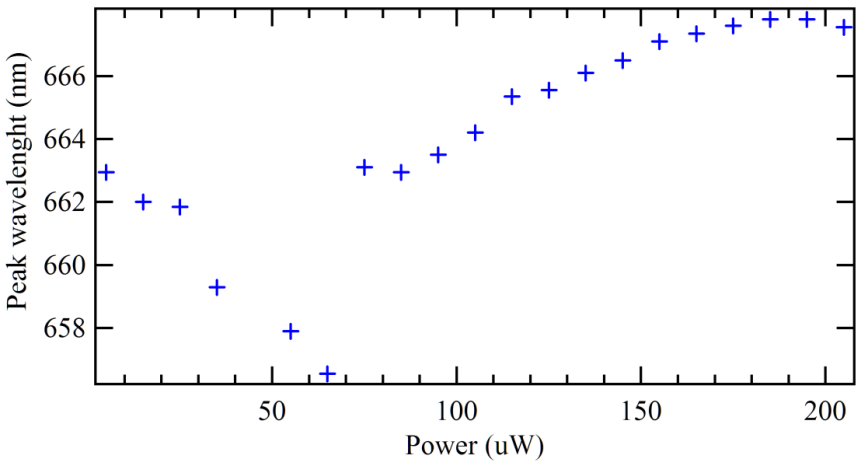

Fig. 4.2.4.4 Pump power vs. peak C central PL emission

Fig. 4.2.4.2 shows the typical laser power dependence characteristic, used also to estimate a laser threshold of 26 μW. After the threshold, lasing regime takes place steadily until a pump power of 160 μW. Then, with the increase of the excitation power, we can see saturation and decreasing of the emission. At the same time is possible to detect another characteristic of lasing regime, the decreasing of the FWHM linewidth plotted in figure 4.2.4.3, where the linewidth of the PL emission decreases from 3nm in the pre-lasing regime to

an average of 1.6nm in the lasing regime. Furthermore a redshift in the emission wavelength, never observed for all the non lasing samples, has been detected. In fig. 4.2.4.4 first a blue shift and then a red shift are easy to spot.

This blue shift has been seen in several other experiments using the same CdSe QDs and photonic crystals. Although there is not an unique expiation yet for this phenomenon, several hypothesis, according the literature, have been proposed. For example in ref. [71] is claimed that the main emission peak shift originates from the recombination of an electron in an s-like state with a hole in an s-like state is blue-shifted and in reference [72] where the relatively strong field of excitation light in PCs is claimed to introduce the DC Stark effect and due to the two-photon excitation energy being above the band gap of CdSe, the optical Stark effect too probably., therefore, the blue shift of TPF spectra of QDs on PCs is mainly attributed to charged exciton emission.

We attribute instead the red shift to the thermo-optical effect of the active material that above 65 μW becomes predominant. It is interesting to notice that only in the lasing sample we observed this redshift. In all the others samples only blue shift has been detected.

Time decay measurement has also been taken for this sample:

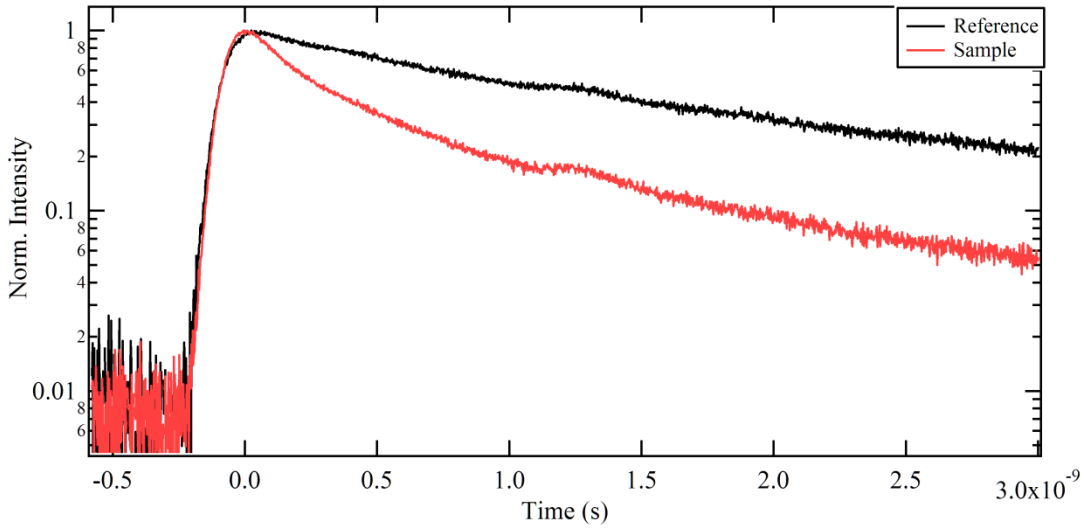

Fig. 4.2.4.5 QDs PL emission time decay curve

Is unmistakable easy to see a much faster decay of the QDs embedded in the SiN nanocavity. The small bump between 1 and 1.5ns can be attributed to a reflection in the setup. Table 4.2.4.1 shows the numerical values of the fitting using a double exponential decay:

	Tau 1 (s)	Tau 2 (s)
Reference	4.41 e-10	1.85 e-9
Sample	2.24 e-10	1.17 e-9

Table 4.2.4.1 Time constants

Looking at the table 4.2.4.1 we can seee a significant change in the time constants especially for the fast component that halve his values due to the Purcell effect. The Q-factor of the nanocavity, calculating fitting the lasing

peak, results to be roughly 400, very close to the 390 predicted theoretically by the PC builder.

4.2.5 Conclusion

As showed in the previous paragraphs, all the indications of lasing regime have been detected in the sample's analysis here presented. Both the power dependence and the linewidth shrinking are present as the most iconic evidence for lasing behavior with a threshold of 26 μW. Moreover is interesting to notice how, among dozens and dozens of samples, only the lasing sample showed the red shift over consolidated lasing regime, meanwhile all the other samples simply showed the blue shift.

4.3 Chapter Conclusion

In this chapter we were able to achieve our goal to use the NCs to realize laser regime in different configurations.

The novel configuration of the uncoated silica microsphere, previously only theoretically predicted to be able to achieve lasing regime, has proved as a valid way to produce lasing. A laser system with uncoated microsphere can

have higher Q-factor then the coated counterparts. They can have much wider tunability over the doped microspheres.

The SiN L3 nanocavity experiment proved as well able to achieve low threshold lasing regime *at room temperature*, as hoped with this family of PCs, even with randomly spincoated QDs embedded in the nanocavity without a precise deposition.

Appendix

In this appendix one more experiment, performed by the author of this work, is described.

The experiment outlines an evanescence technique that uses golden nanoparticle and tapered fiber to measure the absorption spectra of organic molecules with outstanding sensitivity and precision, comparable with a traditional spectrophotometer.

Micro-devices for on chip measurements integrated with photonic components are gaining widespread use in bio-sensing and chemical analysis applications. Incorporating advanced, scaling, highly sensitive photonic devices has the potential to provide compact, effective sensors for lab on a chip tools. Many methods for sensing and analysis have been demonstrated including refraction, absorbance, fluorescence and interferometric measurements [72, 73, 74]. In particular, waveguide-based optical sensing technology appears to be exceptionally amenable to chip integration and miniaturization especially with absorbance-based techniques, particularly

attractive because they offer the potential to provide label-free spectral information for detection and identification of an analyte [75, 76, 77].

Unfortunately the miniaturization of such devices reduces the optical path length for absorption based sensors as compared to macroscopic experiments. A shortened optical path reduces the interaction length of light with a fluid and thus limits the sensitivity of a device and its ability to detect an absorbing species. Several methods have been proposed to mitigate this problem including using slow light in photonic crystals or novel waveguide geometries such a micro-ring resonator [78].

However is this complexity always necessary? In our approach we claim is not and we have developed a technique to perform a miniaturized evanescence field spectroscopy for N-Methylaniline. We used a tapered fiber, to create a strong evanescence field on the tapered region of the fiber, and then coated it with 250 nm diameter golden nanoparticles. Those nanoparticles had a surfactant of polyethylene glycol (PEG) which attracts extremely well the methylaniline molecules, bringing them very close to the fiber and so enhancing the evanescence field absorption of the organic molecule. The experiment schematic is showed in the next figure:

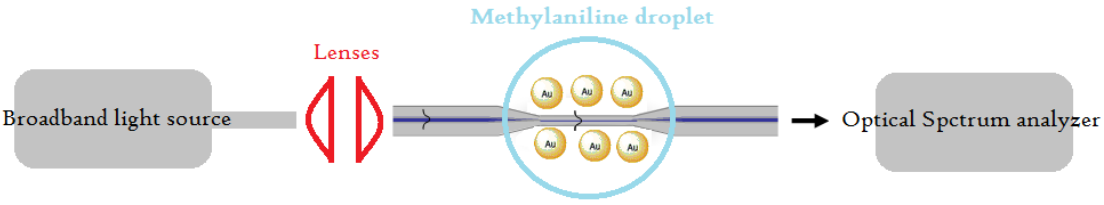

Fig. 5.1 Setup schematic

N-Methylaniline was chosen as molecule for the experiment for several reasons. Is one of the few organic molecule of a known absorption spectra near the 1.5 micron band for optical communication. Is also a secamine in the aniline class and is used as a latent and coupling solvent. Is used as intermediate for dyes, agrochemicals and other organic products manufacturing.

The optical fiber was produce by traditional heat and pull method in the ORC laboratory of Dr. Brambilla. The fiber's core was 2 micron and the fiber was suspended, kept in air under tensile stress buy a specific mount.

The golden nanoparticles were commercial available nano-spheres produced by BBI Solution with a nominal diameter of 250 nm with polyethylene glycol as surfactant.

A broadband light source, with an average power of 1W, was used to excite the sample. The source's emission was focused into the tapered fiber and the fiber connected to an optical spectrum analyzer with a resolution of 1 nm. The N-Methylaniline was diluted in hexane solution with a 3:5 ration. The droplet dropped on the tapered fiber was 1μL.

What we achieved was outstanding and showed in the next graph:

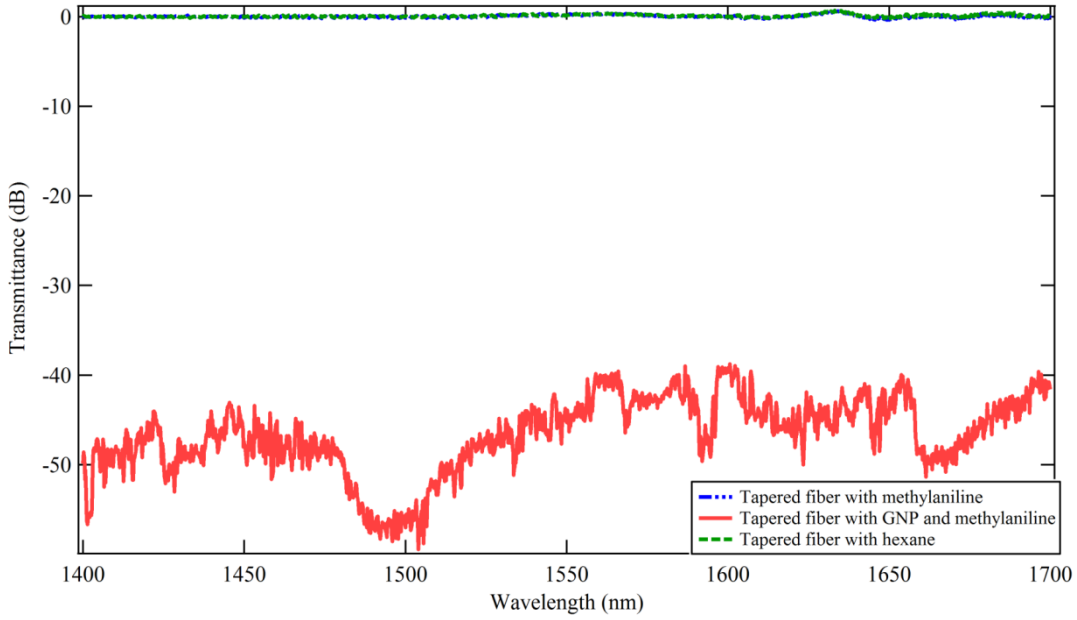

Fig. 5.2 References and absorption spectrum of the N-Methylaniline

The blue and green curves show how the mere presence of the hexane and the methylaniline alone do not affect the transmission in the fiber. However when we coated the tapered fiber with the golden nanoparticles and the methylaniline (red curve) is extremely easy to see the absorption spectra of the organic molecule, centered at 1488 nm with a fitting dip of 12 dB. The transmission drop of almost 48 dB is due the extreme sensitivity of the device and losses introduced by the golden nanoparticles and the organic molecules in the tapered region.

Very interesting is the comparison of the absorption spectrum we obtained with our device and a spectrum, for the same molecule and concentration, taken with a regular spectrophotometer:

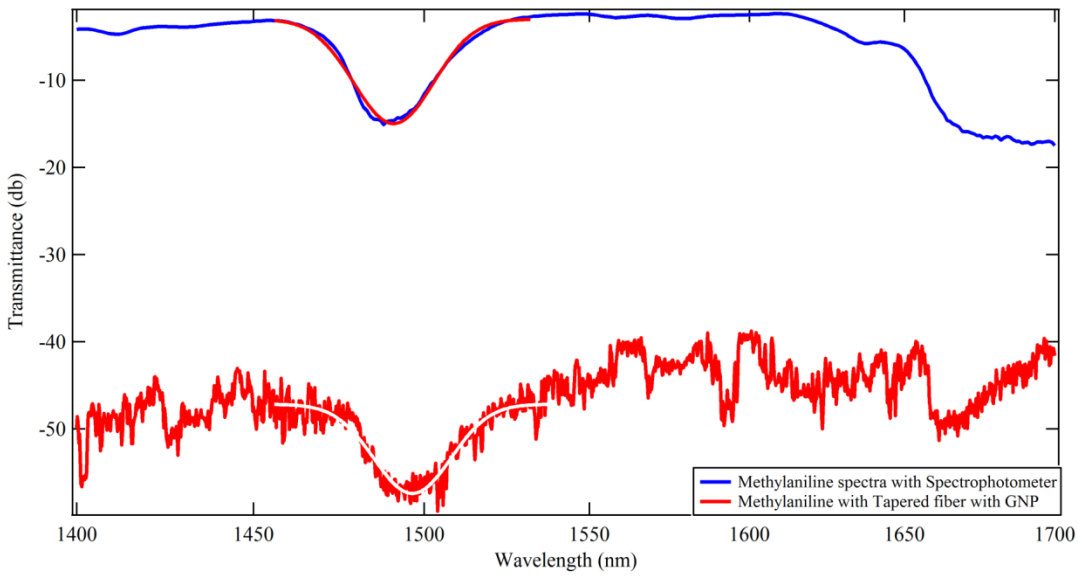

Fig. 5.3 N-Methylaniline spectra taken with our configuration and a regular spectrophotometer

In fig. 5.3 is possible to appreciate how extremely similar, actually almost identical in absolute terms, is the response of our device compare to a classical spectrophotometer. In fact, fitting the two spectra with a Gaussian, we obtain the following table of values:

	Spectrograph	**Tapered fiber**
Curve height (dB)	-11.99 ±0.147	-10.23 ± 0.169
FWHM (nm)	16.73 ± 0.294	16.18 ± 0.429
Central peak (nm)	1491 ±0.138	1496.5 ± 0.222

The height of the fitting and the FWHM is basically identical in the two cases. Only in the central absorption peak there is a difference of 5 nm that can be easily attributed to a different calibration of the instruments.

Conclusion

With this experiment we measured the NIR spectrum of N-Methylaniline using polyethylene glycol ligands (PEG) passivated colloidal gold nanoparticles on tapered fiber. The signal we detected was clear. The advantage of this evanescence field spectroscopy approach is based on the premise that is much simpler to manufacture tapered fiber than waveguide or fancy hybrid structure with resonator embedded in the system when there is no need to use nanoliters of the solution to analyze. In our approach commercial inexpensive nanoparticles combined with a traditional "home-made" tapered fiber were able to detect the absorption spectra of the methylaniline. This could eventually lead to a cheap, mass production, on chip sensing devices, affordable and robust.

Bibliography

[1] R. Rossetti and L. Brus, Electron-hole recombination emission as a probe of surface-chemistry in aqueous CdS colloids, Journal of Physical Chemistry 86, 4470 (1982).

[2] L. E. Brus, Electron-electron and electron-hole interactions in small semiconductor crystallites - the size dependence of the lowest excited electronic state, Journal of Chemical Physics 80, 4403 (1984).

[3] M. G. Bawendi, P. J. Carroll, W. L. Wilson, and L. E. Brus, Luminescence properties of CdSe quantum crystallites: Resonance between interior and surface localized states, The Journal of Chemical Physics 96, 946 (1992).

[4] D. J. Norris, A. Sacra, C. B. Murray, and M. G. Bawendi, Measurement of the Size-Dependent Hole Spectrum in Cdse Quantum Dots, Physical Review Letters 72, 2612 (1994).

[5] W. J. Parak, T. Pellegrino, and C. Plank, Labelling of cells with quantum dots, Nanotechnology 16, R9 (2005).

[6] I. Zutic, J. Fabian, and S. Das Sarma, Spintronics: Fundamentals and applications, Reviews of Modern Physics 76, 323 (2004).

[7] Chia-Hao M. Chuang, Patrick R. Brown, Vladimir Bulović and Moungi G. Bawendi, Improved performance and stability in quantum dot solar cells through band alignment engineering, nature materials, vol 13 August 2014

[8] Weihuang Yang, Jinchai Li, Yong Zhang, Po-Kai Huang, Tien-Chang Lu, Hao-Chung Kuo, Shuping Li, Xu Yang, Hangyang Chen, Dayi Liu & Junyong Kang, High density GaN/AlN quantum dots for deep UV LED with high quantum efficiency and temperature stability, Scientific Reports 4, Article number: 5166

[9] Toshimasa Umezawa, Kouichi Akahane, Naokatsu Yamamoto, Atsushi Kanno and Tetsuya Kawanish, Highly Sensitive Photodetector Using Ultra-High-Density 1.5- μm Quantum Dots for Advanced Optical Fiber Communications, Journal of selected topics in quantum electronics, vol. 20, No. 6, Nov/Dec 2014

[10] DaeGwi Kim, Shinya Okahara, and Masaaki Nakayama, Experimental verification of Förster energy transfer between semiconductor quantum dots, PHYSICAL REVIEW B 78, 153301 2008

[11] Stefan Rohrmoser, Julia Baldauf, Richard T. Harley, and Pavlos G., Lagoudakis, Sameer Sapra and Alexander Eychmüller, Ian M. Watson APL 91, 092126 2007

[12] Investigation of Energy Transfer between CdTe Nanocrystals on Polystyrene Beads and Dye Molecules for FRET-SNOM Applications, Felix Mu1ller, Stephan Go1tzinger, Nikolai Gaponik, Horst Weller, Ju1rgen Mlynek, and Oliver Benson, J. Phys. Chem. B 2004, 108, 14527-14534

[13]Eyal Shafran, Benjamin D. Mangum, and Jordan M. Gerton, Energy Transfer from an Individual Quantum Dot to a Carbon Nanotube, Nano Lett. 2010, 10, 4049–4054

[14] Farbod Shafiei, Sannah P. Ziama, Eric D. Curtis, and Ricardo S. Decca, Measurement of the separation dependence of resonant energy transfer between CdSe/ZnS core/shell nanocrystallite quantum dots, PRB 84, 075301 (2011)

[15] V. Sandoghdar, F. Treussart, J. Hare, V. Lefe`vre-Seguin, J.-M. Raimond, and S. Haroche, Very low threshold whispering-gallery-mode microsphere laser, PRA Volume 54, Number 3 Sep. 1996

[16] M. Cai, O. Painter, P. C. Sercel, and K. J. Vahala, Fiber-coupled microsphere laser, Optics Letter / Vol. 25, No. 19 / October 1, 2000

[17] Matthew Pelton and Yoshihisa Yamamoto, Ultralow threshold laser using a single quantum dot and a microsphere cavity,PRA, Vol. 59, Num. 3 Mar. 1999

[18] Sébastien Steiner, Jean Hare, Valérie Lefêvre-Seguin, and Jean-Michel Gérard, Room temperature lasing of InAs/GaAs quantum dots in the

whispering gallery modes of a silica microsphere, Optics Express, Vol. 15, Issue 16, pp. 10052-10060 (2007)

[19] Christos Grivas, Chunyong Li, Peristera Andreakou, Pengfei Wang, Ming Ding, Gilberto Brambilla, Liberato Manna, & Pavlos Lagoudakis, Single-mode tunable laser emission in the single-exciton regime from colloidal nanocrystals, Nature Communications 4, Article number: 2376

[20] Kuroda, N. Ikeda, T. Mano, Y. Sugimoto, T. Ochiai, K.Kuroda, S. Ohkouchi, N. Koguchi, K. Sakoda, and K.Asakawa, Acceleration and suppression of photoemissionof GaAs quantum dots embedded in photonic crystal microcavities, Appl. Phys. Lett.93, 111103 (2008).

[21] S. Strauf, K. Hennessy, M. T. Rakher, Y. S. Choi, A. Badolato, L. C. Andreani, E. L. Hu, P. M. Petroff, and D. Bouwmeester, Phys. Rev. Lett. 96, 127104 (2006).

[22] T. Uesugi, B. S. Song, T. Asano, and S. Noda, Investigation of optical nonlinearities in an ultra-high-Q Si nanocavity in a two-dimensional photonic crystal slab, Opt. Express14,377–386 (2006).

[23] S. Strauf, K. Hennessy, M. T. Rakher, Y.-S. Choi, A. Badolato, L. C. Andreani, E. L. Hu, P. M. Petroff, and D. Bouwmeester, Self-Tuned Quantum Dot Gain in Photonic Crystal Lasers, Phys. Rev. Lett. 96, 127404

[24] M. M. Makarova, J. Vuckovic, H. Sanda, and Y. Nishi, Silicon-based photonic crystal nanocavity light emitters, Appl. Phys. Lett. 89, 221101 (2006)

[25] M. Barth, J. Kouba, J. Stingl, B. Löchel, and O. Benson, Modification of visible spontaneous emission with silicon nitride photonic crystal nanocavities, Opt. Express 15 , 17231–17240 (2007)

[26] Mohamed M. Murshidy, Ali M. Adawi, Paul W. Fry, David M. Whittaker and David G. Lidzey, The optical properties of hybrid organic–inorganic L3 nanocavities, Vol. 27, No. 2/February 2010/J. Opt. Soc. Am.

[27] Feynmann, R. There is plenty of room at the bottom. Talk, 1959. Annual meeting of the American Physical Society at the California Insitute of Technology

[28] Alivisatos, A. P. Journal of Physical Chemistry, 1996, 100, 13226 - 13239

[29] Mitrin, V. V.; Sementsov, D. I.; Vagidov, N. Z. Quantum Mechanics for Nanotructures. Cambridge University Press, Cambridge, 2010.

[30] Brus, L. E. J. Chem. Phys., 1984, 80, 4403 – 4409

[31] Blachnik, R.; Chu, J.; Galazka, R. R.; Geurts, J.; Gutowski, J.; Hönerlage, B.; Hofmann, D.; Kossut, J.; Lèvy, R.; Michler, P.; Neukirch, U.; Strauch, D.; Story, T.; Waag, A. Landolt-Börnstein: Group III:

Condensed Matter, Volume41 Semiconductors, Subvolume B, II - VI and III - V Compounds, Semimagnetic compounds. Springer- Verlag, Berlin, Heidelberg, New York, 1999

[32] C. B. Murray, C. R. Kagan, M. G. Bawendi, Synthesis and characterization of monodisperse nanocrystals and close-packed nanocrystal assemblies, Annu. Rev. Mater. Sci. 2000. 30:545–610

[33] Luigi Carbone, Concetta Nobile, Milena De Giorgi, Fabio Della Sala, Giovanni Morello, Pierpaolo Pompa, Martin Hytch, Etienne Snoeck, Angela Fiore, Isabella R. Franchini, Monica Nadasan, Albert F. Silvestre, Letizia Chiodo, Stefan Kudera, Roberto Cingolani, Roman Krahne, and Liberato Manna, Synthesis and Micrometer-Scale Assembly of Colloidal CdSe/CdS Nanorods Prepared by a Seeded Growth Approach, NANO LETTERS 2007 Vol. 7, No. 10, 2942-2950

[34] Cairo, G. (1922). Uber Entstehung wahrer Lichtabsorption und scheinbare Koppelung von Quantenspru¨ngen. Z. Phys. 10, 185–99

[35] Cairo, G. and Frank, J. (1922). Uber Zerlegugen von WasserstoVmoleku ¨len durch angeregte Quecksilberatome. Z. Phys. 11, 161–6

[36] Perrin, F. (1933). Interaction entre atomes normal et activite´. Transferts d'activitation. Formation d'une molecule activite´e. Ann. Institut Poincare´ 3, 279–318.

[37] Perrin, J. (1927). Fluorescence et induction moleculaire par resonance. C. R. Hebd. Seances Acad. Sci. 184, 1097–100.

[38] Robert M. Clegg, Foerster resonance energy transfer—FRET what is it, why do it, and how it's done, Laboratory Techniques in Biochemistry and Molecular Biology, Volume 33 FRET and FLIM Techniques T. W. J. Gadella (Editor)

[39] Foerster, T. (1946). Energiewanderung und Fluoreszenz. Naturwissenschaften 6, 166–75.

[40] Hans Kuhn, 1970 The Journal of Chemical Physic, Volume 53, Number

[41] Uber Glatte und Ebenheit als physikalisches und physiologishes Problem, Gustev Shmalz, Verein Deutscher Ingenieure, Oct 12, 1929, pp. 1461-1467

[42] U.S. Patent 2,728,222

[43] UK Patent 2,009,409

[44] R. Young, J. Ward, F. Scire, The Topografiner: An Instrument for Measuring Surface Microtopography, Rev. Sci. Inst., Vol 43, No 7, p 999

[45] G. Binnig, H. Rohrer, Ch. Gerber, E. Weibel, Surface Studies by Scanning Tunneling Microscopy, Vol. 49, No 1, 1982, p 57

[46] G. Binnig, C.F. Quate, Ch. Geber, Atomic Force Microscope, Phys. Rev. Letters, Vol. 56, No 9, 1986 p 930

[47] Paul E. West, Introduction To Atomic Force Microscopy

[48] Y. Martin, C.C. Williams, H.K. Wickramasinghe, Atomic Force Microscope-Force Mapping and Profiling on a sub 100-E scale. J. Appl. Phys. Vol 61, No 10, 1987, p 4723

[49] Wolfang Becker, the TCSPC handbook

[50] K. Yamaguchi, M. Fujii, M. Haraguchi, T. Okamoto, and M. Fukui, Opt. Express 17, 23204 (2009).

[52] F. Vollmer, S. Arnold, and D. Keng, Proc. Natl. Acad. Sci. 105, 20701 (2008)

[53] Min, B. et al. Ultralow threshold on-chip microcavity nanocrystal quantum dot CdSe/ZnS laser. Appl. Phys. Lett. 89, 191124 (2006).

[54] Eisler, H.-J. et al. Color-selective semiconductor nanocrystal laser. Appl. Phys. Lett. 80, 4614–4616 (2002).

[55] Christos Grivas, Chunyong Li, Peristera Andreakou, Pengfei Wang, Ming Ding, Gilberto Brambilla, Liberato Manna, Pavlos Lagoudakis, Nature Communications 4, Article number: 2376 (2013)

[56] G. C. Righini, Y. Dumeige, P. Féron, M. Ferrari, G. Nunzi Conti, D. Ristic, and S. Soria, "Whispering gallery mode microresonators: Fundamentals and applications," Rivista del Nuovo Cimento 34(7) (2011).

[57] Y. P. Rakovich and J. F. Donegan, "Photonic atoms and molecules," Laser Photon. Rev. 4(2), 179–191 (2009) [doi:10.1002/lpor.200910001].

[58] M. Benson, S. V. Boriskina, P. Sewell, A. Vukovic, S. C. Greedy, and A. I. Nosich, "Micro-optical resonators for microlasers and integrated optoelectronics: recent advances and future challenges," in arXiv physics.optics (2006).

[59] Vladimir S. Ilchenko, X. Steve Yao, and Lute Maleki, Pigtailing the high-Q microsphere cavity: a simple fiber coupler for optical whispering-gallery modes, June 1, 1999 / Vol. 24, No. 11 / OPTICS LETTERS

[60] S. Strauf, K. Hennessy, M. T. Rakher, Y. S. Choi, A. Badolato, L. C. Andreani, E. L. Hu, P. M. Petroff, and D. Bouwmeester, Phys. Rev. Lett. 96, 127104 (2006).

[61] Mohamed M. Murshidy, Ali M. Adawi, Paul W. Fry, David M. Whittaker, and David G. Lidzey, Vol. 27, No. 2/February 2010/J. Opt. Soc. Am. B

[62] Lord Rayleigh, the Propagation of Waves through a Medium Endowed with a Periodic Structure, Philosopical Magazine 1887

[63] V. P. Bykov, Spontaneous emission in a periodic structure, Sov. Phys. JETP 35, 269-273 (1972).

[64] E. Yablonovitch, Phys. Rev. Lett. 58, 2059 (1987)

[65] S. John, Phys. Rev. Lett. 58,2486 (1987)

[66] K. M. Ho, C. T. Chan, C. M. Soukoulis, "Existence of a photonic gap in periodic dielectric structures," Phys. Rev. Lett. 65, 3152 (1990).

[67] H. S. Sözüer, J. W. Haus, and R. Inguva , Photonic bands: Convergence problems with the plane-wave method, Phys. Rev. B 45, 13962 – Published 15 June 1992

[68] S. Noda, K. Tomoda, N. Yamamoto, and A. Chutinan, "Full three-dimensional photonic bandgap crystals at nearinfrared wavelengths," Science 289(5479), 604–606 (2000)

[69] S. G. Johnson and J. D. Joannopoulos, "Introduction to Photonic Crystals: Bloch's Theorem, Band Diagrams, and Gaps (But No Defects)" (2003)

[70] M. C. Troparevskya and A. Franceschetti, APL 87, 263115 2005

[71] Xingsheng Xu, Scientific report | 3 : 3228 | DOI: 10.1038/srep03228

[72] Xingsheng Xu, Enhanced trion emission from colloidal quantum dots with photonic crystals by two-photon excitation, SCIENTIFIC REPORTS | 3 : 3228 | DOI: 10.1038/srep03228

[73] J. Dostalek, J. Ctyroky, J. Homola, E. Brynda, M. Skalsky, P. Nekvindova, J. Spirkova, J. Skvor, and J. Schrofel, Sens. Actuators B 76, 8-12 (2001).

[74] M. L. Chabinyc, D. T. Chiu, J. C. McDonald, A. D. Stroock, J. F. Christian, A. M. Karger, and G. M. Whitesides, Anal. Chem. 73, 4491-4498 (2001).

[75] B Sepulveda, J S´anchez del Rio, Moreno F J Blanco, KMayora, C Dominguez L M Lechug, Optical biosensor microsystems based on the integration of highly sensitive Mach–Zehnder interferometer devices, J Opt. A: Pure Appl. Opt. 8 (2006) S561–S566

[76] András Székács, Nóra Adányi2 Inna Székács, Krisztina Majer-Baranyi, István Szendrő, Optical waveguide light-mode spectroscopy immunosensors for environmental monitoring, 1 February 2009 / Vol. 48, No. 4 / APPLIED OPTICS

[77] Adam L. Washburn, L. Cary Gunn, d Ryan C. Bailey, Label-Free Quantitation of a Cancer Biomarker in Complex Media Using Silicon Photonic Microring Resonators , Anal. Chem. 2009, 81, 9499–9506

[78] Arthur Nitkowski, Long Chen, Michal Lipson, Cavity-enhanced on-chip absorption spectroscopy using micro-ring resonators, 4 August 2008 / Vol. 16, No. 16 / OPTICS EXPRESS 11930

[79] https://en.wikipedia.org/wiki/Atomic_force_microscopy. This work has been released into the public domain by its author, OverlordQ at the English Wikipedia project. This applies worldwide. OverlordQ grants

anyone the right to use this work for any purpose, without any conditions, unless such conditions are required by law.

[80] http://www.adsdyes.com/products/ADS129BE.html